

# Quantum Dots Microstructural Metrology: From Time-Resolved Spectroscopy to Spatially Resolved Electron Microscopy

Hasna Kudilatt, Bo Hou,\* and Mark E. Welland\*

Colloidal quantum dots (QDs) have unique optical and electrical properties with promising applications in next-generation semiconductor technologies, including displays, lighting, solar cells, photodetectors, and image sensors. Advanced analytical tools to probe the optical, morphological, structural, compositional, and electrical properties of QDs and their ensemble solid films are of paramount importance for the understanding of their device performance. In this review, comprehensive studies on the state-of-the-art metrology approaches used in QD research are introduced, with particular focus on time-resolved (TR) and spatially resolved (SR) spectroscopy and microscopy. Through discussing these analysis techniques in different QD system, such as various compositions, sizes, and shell structures, the critical roles of these TR-spectroscopic and SR-microscopic techniques are highlighted, which provide the structural, morphological, compositional, optical, and electrical information to precisely design QDs and QD solid films. The employment of TR and SR analysis in integrated QD device systems is also discussed, which can offer detailed microstructural information for achieving high performance in specific applications. In the end, the current limitations of these analytical tools are discussed, and the future development of the possibility of interdisciplinary research in both QD fundamental and applied fields is prospected.

## 1. Quantum Dots

Quantum dots (QDs) have gained broad acceptance, applicability, and much interest in current semiconductor technology due to their unique optical and electrical properties.<sup>[1,2]</sup> QDs are semiconductors with size between 3 and 20 nm where electron and hole wave functions are highly confined.<sup>[3]</sup> The dimension should be comparable to the Bohr exciton radius of the material, and that leads to discrete energy levels in QD. QDs are attracted by their unique atomic-like narrow emission that can be tuned easily by controlling their size, structure, and composition.<sup>[4–6]</sup> The optical and electrical properties of QDs are better than organic fluorophores. For instance, QD has high quantum efficiency, excellent color gamut, narrow emission bandwidths, broad color tunability, high photostability, and high air stability.<sup>[7]</sup> These excellent properties make QD a potential candidate for applications in various fields such as optoelectronics, sensing, and imaging.<sup>[1,8–10]</sup>

QDs are typically composed of group II–VI, III–V, and IV–VI compound semiconductors such as CdS, CdSe, PbS, ZnS, InAs, and ZnInS.<sup>[11–16]</sup> Because of minimal particle diameter, QDs have a high surface-to-volume ratio, and these surface trap states act as centers for nonradiative transitions that diminish the performance of QDs. This can be overcome by the growth of inorganic shells such as ZnS, CdTe, and CdSe. Various core–shell QDs such as CdSe/ZnS, CdSe/CdS/ZnS, CdTe/CdSe, InAs/CdSe, InP/ZnS, PbSe/PbS, and InP/GaP/ZnS have been already developed.<sup>[17–25]</sup> In addition to the improved surface stability, the growth of shell over the QD core enhanced the luminescence quantum efficiency and exciton lifetime as compared with the behavior seen in the cores. Core–shell heterostructures also provide an opportunity to tune their electronic properties via the band edge alignment.<sup>[26]</sup> Tailoring the properties of core–shell QDs concerning their shape leads to the development of anisotropic structures such as rod, disc-like, teardrop, and tetrapod structures and in which core–shell tetrapods composed of metal chalcogenide semiconductors have gained much more attention due to the multiple functionalities that arise from their branched geometry structure.<sup>[27–29]</sup>

Dr. H. Kudilatt, Prof. M. E. Welland  
Nanoscience Centre  
Department of Engineering  
University of Cambridge  
Cambridge CB3 0FF, UK  
E-mail: mew10@cam.ac.uk

Dr. H. Kudilatt, Prof. M. E. Welland  
Electrical Engineering Division  
Department of Engineering  
University of Cambridge  
9 JJ Thomson Avenue, Cambridge CB3 0FA, UK

Dr. B. Hou  
School of Physics and Astronomy  
Cardiff University  
Cardiff, Wales CF24 3AA, UK  
E-mail: houb6@cardiff.ac.uk

 The ORCID identification number(s) for the author(s) of this article can be found under <https://doi.org/10.1002/ppsc.202000192>.

© 2020 The Authors. Published by Wiley-VCH GmbH. This is an open access article under the terms of the Creative Commons Attribution License, which permits use, distribution and reproduction in any medium, provided the original work is properly cited.

DOI: 10.1002/ppsc.202000192

## 1.1. Electronic States and Carrier Dynamic Properties of QDs

As a consequence of quantum confinement in QD semiconductors, the continuous energy band alters to discrete energy, and it is more pronounced in QDs whose size is smaller than Bohr exciton radius. These discrete energy levels of electrons are designated using quantum numbers “*n*” and “*L*,” but there is no restriction in the value of *L*, unlike hydrogen atom. Hence, the lowest energy levels of electrons are 1S, 1P, 1D, 2S, etc. in the order of increase in energy and the quantum confinement effect can be observed in absorption and emission spectra of QDs.<sup>[30]</sup> Due to the multi-subband character of the valence band (VB) and their coupling, the energy levels of holes are termed as 1S<sub>3/2</sub>, 1P<sub>3/2</sub>, 2S<sub>3/2</sub>, etc.<sup>[31]</sup> The lowest energy transition is 1S<sub>3/2</sub>(h)–1S(e) and the hole in the VB and electron in the conduction band (CB) forms a pair termed as “exciton.” Exciton is characterized by their lifetime, and the path followed by the exciton during recombination crucially determines the efficiency of QD-based devices. The possible processes involved during recombination of exciton are discussed in the following sections.<sup>[29,30,32–34]</sup>

### 1.1.1. Exciton Relaxation

Upon excitation with light or voltage, an electron in the VB is promoted to the energy levels of the CB leaving a hole in VB to form an exciton. If the incident energy is large, the electron and hole occupy levels higher than the lowest level, 1S and these hot excitons follow an intraband transition to release its excess energy. During the intraband transition, the excess energy of electron and hole is released as heat through electron–phonon interaction, and the electron reaches to the bottom of the CB and hole reaches to the top of VB. The time of scale of this intraband transition is of the order of several tens to hundreds of femtosecond (fs).

### 1.1.2. Exciton Recombination

After the intraband transition, electron and hole can be recombined to emit a photon known as band edge emission or make the nonradiative transition that produces heat.<sup>[32]</sup> In an ideal QD, the primary recombination will be radiative, and the quantum yield is very high, and the excitons have a lifetime of the order of nanoseconds (ns). In a typical QD, the density of trap states is high, and thus the nonradiative transition to these trap state is significant, and these processes occur in a timescale of few picosecond (ps) to few tens of ps. Trapping of one of the charge carriers at surface states causes strong carrier localization and competes with radiative recombination and leads to luminescence quenching. Depending on the nature of trap states, the trapped electron follows radiative or nonradiative transition. The electron can move from shallow state to deeper trap states, and these states are long-lived, and their lifetime is varied from few tens of ps to microseconds. It is facilitated by coupling to local vibrations, and the recombination will be without emitting a photon. The radiative transition spectra associated with trapping states (known as trap-state PL), are broad and red-shifted as compared to band edge emission, and thus can be easily distinguished. Because of as-mentioned possible processes, the observed lifetime of exciton will be a combination of a radiative and nonradiative lifetime and related as follows<sup>[33]</sup>

$$\frac{1}{\tau} = \frac{1}{\tau_r} + \frac{1}{\tau_{nr}} \quad (1)$$

where  $\tau_r$  and  $\tau_{nr}$  are the radiative and the nonradiative lifetimes, respectively. The excitation of exciton and the possible recombination pathways are schematically represented in Figure 1a.

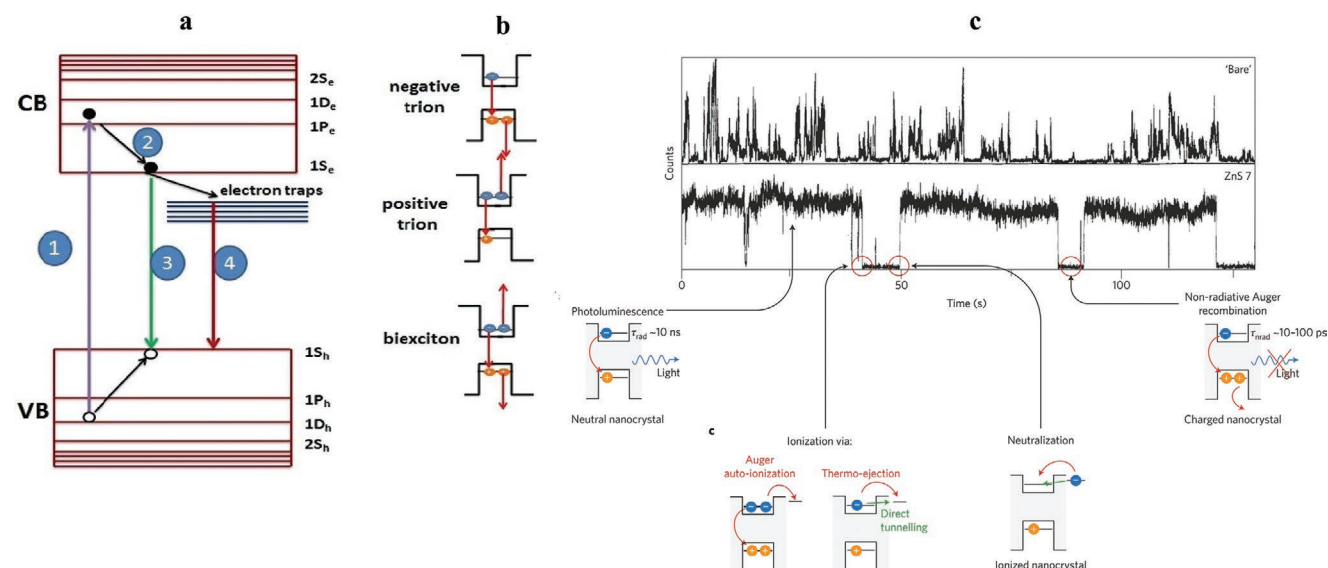


**Figure 1.** a) 1) Formation of exciton; 2) the intraband transition of exciton; 3) radiative recombination; and 4) trap-assisted radiative recombination of the exciton. b) Nonradiative Auger recombination in positive trion, negative trion, and biexciton. c) The time dependence of the PL intensity of a single CdSe QD without and with ZnS shell (top); schematics of various radiative and nonradiative processes corresponding to ON and OFF state in the PL trace (bottom). Reproduced with permission.<sup>[39]</sup> Copyright 2016, Nature.

### 1.1.3. Auger-Assisted Recombination

Normally, nonradiative recombination of excitons resulted in thermalization and released energy in the form of heat. When the intensity of light is high or under constant illumination, density of excited charge carriers or excitons is very high that leads to the observation of nonlinear dynamical processes such as Auger recombination or exciton–exciton annihilation.<sup>[31,32,35,36]</sup> The forced overlapping electron wave function strengthens the carrier–carrier interaction via Coulomb interaction that really affect its dynamics. The significant process that affects PL quantum yield (PLQY) of QD is Auger recombination during which an extra electron or hole promoted to higher energy states consuming energy from excited exciton and rate of Auger-assisted recombination can be orders of magnitude faster than that of radiative recombination. The excited state can be either a bound state or a continuum state. The multi-carrier states that encourage Auger recombination are charged trion or biexciton, and depending on the nature of multicarrier states, the pathway of Auger recombination is schematically given in Figure 1b.<sup>[37]</sup> For an excellent detailed review of spectral and dynamical properties of multiexcitons in QDs, the readers are referred to the study by Klimov.<sup>[31]</sup>

It is identified that this Auger recombination process causes “PL blinking” at a single-QD level.<sup>[38]</sup> PL blinking is the random switching between higher (ON) and lower (OFF) PL emissivity and is observed as a sequence of ON and OFF period in the time dependence PL intensity trace.<sup>[39]</sup> This blinking due to charging and discharging of charged QDs is termed as A-type blinking. The second type of blinking, B-type, is also observed in QDs, and it is due to the charge fluctuations in the surface trap states because of tunneling of hot electrons under photoexcitations. A-type and B-type can be differentiated as follows: in conventional (A-type) blinking, the decrease in PL intensity during blinking occurs simultaneously with shortening of the PL lifetime. Nevertheless, in B-type, the decrease of PL intensity occurs without changing in the PL lifetime. The processes involved during blinking mechanism are well explained in the report by Efros and Nesbitt and the PL trace of CdSe and CdSe/ZnS QDs and the processes occurrence during ON and OFF are given in Figure 1c.<sup>[39]</sup>

The photoexcitation and the exciton recombination in hetero-nanostructures such as core–shell QDs are more complicated as compared to single composition because of the energy level alignment between the materials.<sup>[40–42]</sup> Depending

on the offsets of CB and VBs of two adjoining materials, localization of electron and hole after excitation will be different. According to the carrier localization, core–shell QDs are classified as type-I, type-I<sub>1/2</sub> (also referred to as quasi-type-II), and type-II.<sup>[30,43]</sup> In type-I system, the core could have a smaller bandgap than the shell such that both carriers are confined within the core.

In contrast, type-II is characterized such that the CB or VB of the core is located within the bandgap of the shell that resulted in a staggering bandgap alignment of the core and the shell. The staggered alignment in type-II leads to the separate allocation of the two carriers in the core and the shell. If the CB or the VB offset in type-II is small, one of the carriers spreads over the entire QD while confining the other either in the core or in the shell, and this is referred to as a quasi-type-II system.

### 1.2. QDs in Optoelectronics and Photonics

A significant number of researches have been carried out to utilize QDs in a range of optoelectronic applications including next-generation smart displays/lightings, solar cells, photodetectors, and image sensors.<sup>[1,36,44–47]</sup> QD backlight LCDs are readily commercialized and available in the market since 2015.<sup>[48]</sup> **Figure 2** presents the first demonstrated flexible quantum dot light-emitting diode (QLED) display using CdSe/CdS/ZnS QDs by a solvent-free transfer printing technique. Large-area, electroluminescent-mode, full-color QD displays having a competent performance with organic LED displays have been demonstrated as a breakthrough in the display industry.<sup>[49]</sup> Bandgap tunability to solar spectrum makes QD one of the potential candidates for the multiple junction solar cells. Recently, Hou et al. reported the fabrication of high-performance cascaded-junction QD solar cells using highly monodispersed PbS QDs and Choi et al. fabricated homogeneous colloidal QD (CQD) bulk homojunction photovoltaics with highest power conversion efficiency.<sup>[50,51]</sup> Solar cell performance in photovoltaic devices employing PbS QDs bulk homojunction films are given in **Figure 3a–c**.

Development of IR photodetectors using solution-processed colloidal semiconductor nanocrystals as active material is a very active area of research.<sup>[52,53]</sup> The QD-based photodetectors are advantageous because of the economical fabrication approach, and it can be integrated with a plethora of different substrates. An efficient IR photodetector has been fabricated

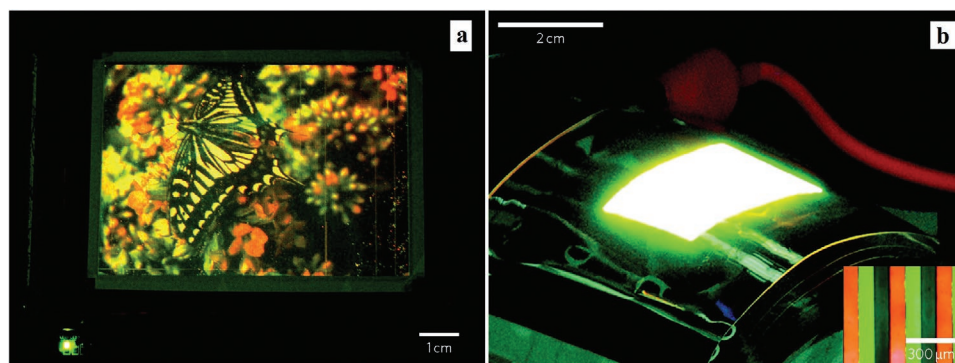


**Figure 2.** a) Electroluminescence image of a 4 in. full-color QLED display using CdSe/CdS/ZnS QD and b) flexible QLED with RGB QDs patterned by a solvent-free transfer printing technique. Reproduced with permission.<sup>[49]</sup> Copyright 2011, Springer Nature.

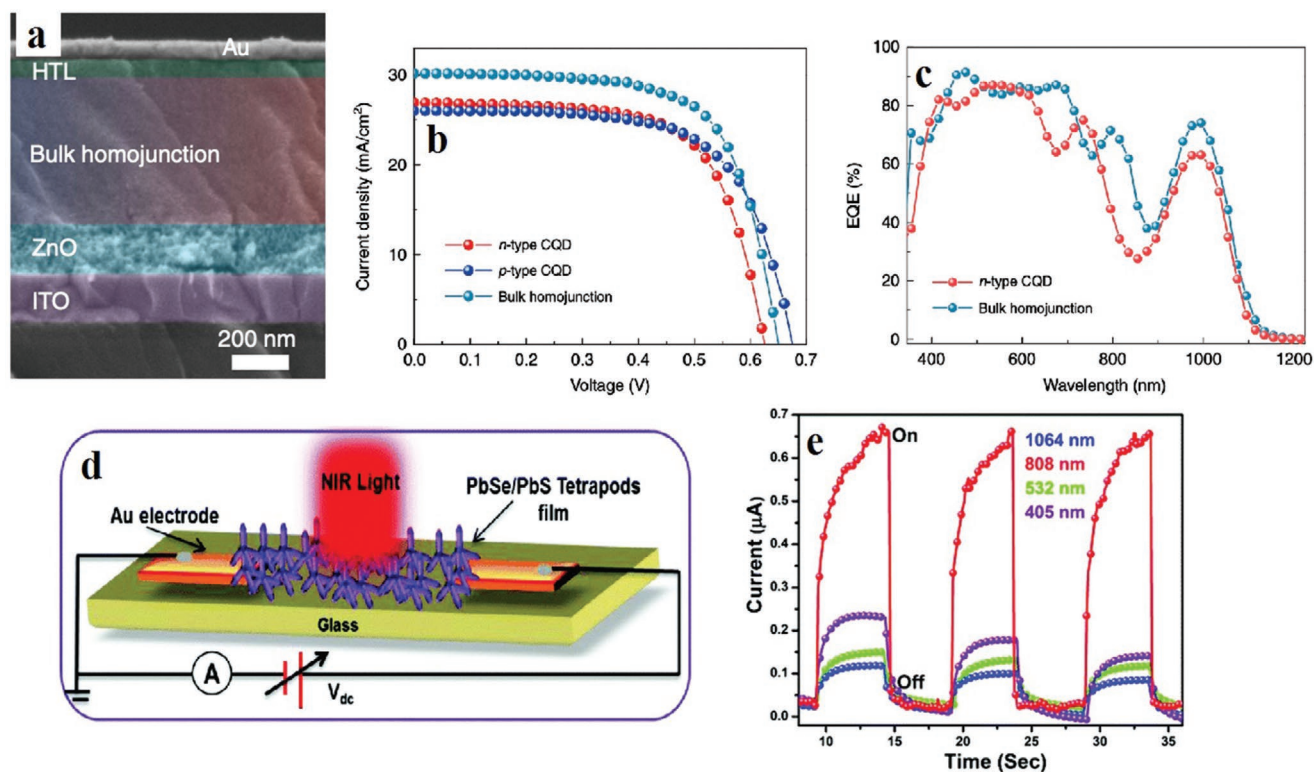


**Figure 3.** a) Cross-sectional scanning electron microscopy image of PbS QD bulk homojunction device. b) Current–voltage characteristics under AM1.5 illumination for bulk homojunction devices and p-type and n-type CQDs. c) External quantum efficiency of n-type CQD device and bulk homojunction device. Reproduced with permission.<sup>[51]</sup> Copyright 2020, Springer Nature. d) Schematic of the PbSe/PbS tetrapod-based IR photodetector. e) The temporal response of photodetector at different excitations. Reproduced with permission.<sup>[29]</sup> Copyright 2016, The Royal Society of Chemistry.

by Mishra and co-workers using PbSe-seeded PbS tetrapods as an active material.<sup>[29]</sup> The schematic of tetrapod-based IR photodetector and its temporal response for different excitation light are given in Figure 3d,e. QDs have also been widely applied in biosensing, bioimaging, and drug delivery and the advancement of QD biomedical applications made the possibility of real-time monitoring of the occurrence and development of diseases in living organisms.<sup>[54]</sup> Li et al. carried out in vivo imaging of traumatic brain injury using Ag<sub>2</sub>S-based nanoprobe<sup>[55]</sup> and Lv and co-workers developed “all-in-one” theranostic nanomedicines having intrinsic imaging and

therapeutic capabilities within a well-defined nanostructure using CuInS/ZnS QDs (ZCIS QDs).<sup>[56]</sup> The synthesized ZCIS QD were successfully employed for fluorescence/multispectral optical tomography (MSOT) dual-modal imaging and photothermal therapy and photodynamic therapy (PTT/PDT)-mediated tumor ablation (Figure 4).

### 1.3. SR and TR Tools for QD Metrology

Steady efforts have been dedicated in synthetic strategy, surface passivation, and core–shell interface composition design for the generation of desirable QDs with improved physical, chemical, and biological properties suitable for specific applications.<sup>[57–59]</sup> These advancements in the development of efficient QDs remind the necessity of potential analytical techniques to track the QD formation and to probe structural, morphological, compositional, optical, and electronic properties of the developed QDs for exploiting their applications in a number of technological fields, including display technology, solar energy conversion, optical detectors, sensors, and many others. Various TR and SR spectroscopic and microscopic tools with high temporal and spatial resolution have been developed by combining well-established techniques to characterize both static and dynamic properties of QDs.<sup>[60–63]</sup> Microscopic techniques are used to determine the properties such as size, crystalline structure, chemical composition, electronic states, and work function. The spatial

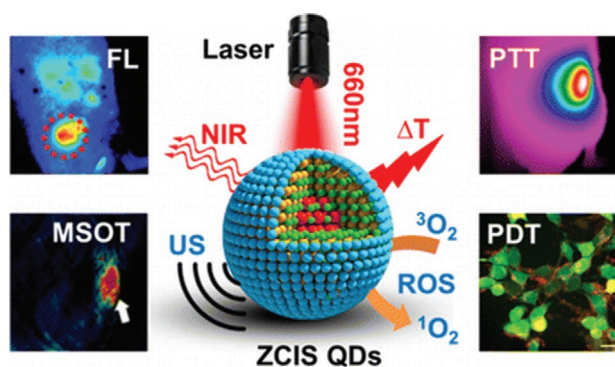


**Figure 4.** Illustration of ZCIS QDs used as “all-in-one” theranostic nanomedicines with intrinsic fluorescence/MSOT imaging and PTT/PDT therapeutic capabilities. Reproduced with permission.<sup>[56]</sup> Copyright 2016, The American Chemical Society.

resolution of the instrument controls the success of this measurement. Hence, electron beam (e-beam) and X-rays are used to map composition, structure, and morphology of QDs with high resolution.<sup>[64]</sup> Development of probe-based imaging techniques further improved the spatial resolution down to a single atom.<sup>[65–67]</sup> The TR studies have been carried out on QDs both to track the growth mechanism and also to investigate the relaxation pathways and lifetime of exciton that play a crucial role in the performance of QD-based devices.<sup>[32,68]</sup> Combination of TR and SR techniques gave more insight into the fundamental properties of QDs. In this review, we highlight the progress in TR and SR spectroscopic and microscopic tools that have been employed for the investigation of QD properties and their performances.

## 2. TR Spectroscopy

TR studies in QDs are essential to determine the lifetime of charge carriers and their associated relaxation pathways. Since exciton lifetime is very short, ultrafast laser techniques are employed to monitor their lifetime and associated relaxation or recombination processes.<sup>[69]</sup> Ultrafast laser techniques such as transient absorption spectroscopy (TAS) and time-resolved photoluminescence (TRPL) spectroscopy are the well-known tools used to monitor processes such as exciton dynamics, charge/energy transfer, and multiexciton generation phenomena in QDs measurements.<sup>[70–78]</sup> TRPL and TAS can reveal the evolution of excited states in a nanosecond to fs timescale. In TRPL, the time evolution is measured by monitoring emission from the QDs. In contrast, in TAS, the time evolution is measured by monitoring the absorption.

### 2.1. Time-Resolved Photoluminescence

TRPL spectroscopy probes the excited-state population in QDs. It reveals the time-dependent photoemission rates from one or more radiative excited states. During measurement, a short pulse of light generates electron–hole pairs that decay to lower energy levels of the sample depending on the lifetime of each excited states. Subsequently, these electron–hole pairs are recombined, and light is emitted. The emitted light is composed of a set of wavelengths corresponding to the transition energies and, as a result, measurement of the optical spectrum as a function of time provides ways to measure the transition energies and their lifetimes. Photomultiplier tube (PMT), photodiode, or charge-coupled device (CCD) is used to monitor the time profile of the PL. The temporal resolution of the measurement is determined by the detector, which is usually of the order of ps or ns and is longer than excitation laser pulse. TRPL studies at single-QD level can be performed by time-correlated single-photon counting (TCSPC) method and its instrument's resolution is in the order of 25 ps. The primary benefit of TCSPC is its higher sensitivity that allows both ensemble and single-QD PL measurement. Other methodologies exist, involving luminescence upconversion, TR fluorescence, four-wave mixing, and terahertz time-domain spectroscopy.<sup>[79–83]</sup>

Even though TRPL records transient population correspond to radiative recombination of charge carriers, PL decay curves are

multiexponential because of the several competing radiationless processes including carrier trapping, charge transfer, etc. Hence, the analysis of PL decay curve is complex. With the support of an appropriate theoretical model, multiexponential fitting of PL decay curve helps to calculate the average PL lifetime and radiative and nonradiative transition rates in QDs.<sup>[73]</sup> The triexponential model to fit the PL decay curve is given by Equation (2)<sup>[84]</sup>

$$F(t) = A + \alpha_1 \exp\left(-\frac{t}{\tau_1}\right) + \alpha_2 \exp\left(-\frac{t}{\tau_2}\right) + \alpha_3 \exp\left(-\frac{t}{\tau_3}\right) \quad (2)$$

where  $\tau_1$ ,  $\tau_2$ , and  $\tau_3$  represent the lifetimes and  $\alpha_1$ ,  $\alpha_2$ , and  $\alpha_3$  represent the corresponding pre-exponential functions, respectively. Out of these three-lifetime components, short component corresponds to band edge excitons or single exciton, and fast component corresponds to charged exciton.<sup>[85,86]</sup> The component  $\tau_3$  can be attributed to the deep trap site (i.e., defect states). The power-dependent fluorescence lifetime measurements help to confirm these lifetime assignments in which the fast component increases with power, the medium component decreases with power, and the slowest component shows very little power dependence.<sup>[87]</sup>

The average lifetime ( $\tau_{av}$ ) radiative transition rate  $\langle k_r \rangle$  and nonradiative transition rate  $\langle k_{nr} \rangle$  can be calculated using Equations (3–5), respectively

$$\tau_{av} = \frac{\alpha_1 \tau_1^2 + \alpha_2 \tau_2^2 + \alpha_3 \tau_3^2}{\alpha_1 \tau_1 + \alpha_2 \tau_2 + \alpha_3 \tau_3} \quad (3)$$

$$\langle k_r \rangle = \frac{QY}{\tau_{av}} \quad (4)$$

$$\langle k_{nr} \rangle = \frac{1}{\tau_{av}} - k_r \quad (5)$$

Criteria for a high-performance QD-based device are the high PLQY and long PL lifetime in the QD film. Generally, when QDs are transferred from the solution phase to solid film, their PLQY and PL lifetime is reduced due to the Förster resonance energy transfer (FRET).<sup>[88,89]</sup> The probability of FRET strongly depends on the distance between the interacting QD dipoles and TRPL is an effective tool to assess the FRET efficiency. **Figure 5a** compares TRPL spectra of ZnCdSe/ZnS//ZnS QD solution with that of solid film, and it can be observed that PL decay becomes faster due to the closed-packed QDs in solid film state. The shell, a nontrivial energy barrier, can act as an effective spacer in core–shell QD films to inhibit FRET by reducing leakage current. Hence, the probability of FRET can be progressively reduced by increasing shell thickness.<sup>[90]</sup> TRPL measurement can also give insight into the charge balance at QD/charge transport layer interface (CTL) in QLED device.<sup>[91,92]</sup> Effect of the insulating layer to improve PL lifetime of devices by suppressing spontaneous charging of QDs at the interface is investigated in QLED devices. Li and co-workers fabricated ZnCdSe/ZnS//ZnS-based QLED with PMMA as an insulating layer. They confirmed that PL lifetime is improved as compared with that without PMMA (**Figure 5b**).<sup>[89]</sup> Hollingsworth and co-workers performed TRPL using TCSPC on InP/CdS QDs to estimate average PL lifetime and employed pump power-dependent TRPL using spectrograph and photon-counting streak camera to estimate biexciton lifetimes.<sup>[93]</sup> The effect

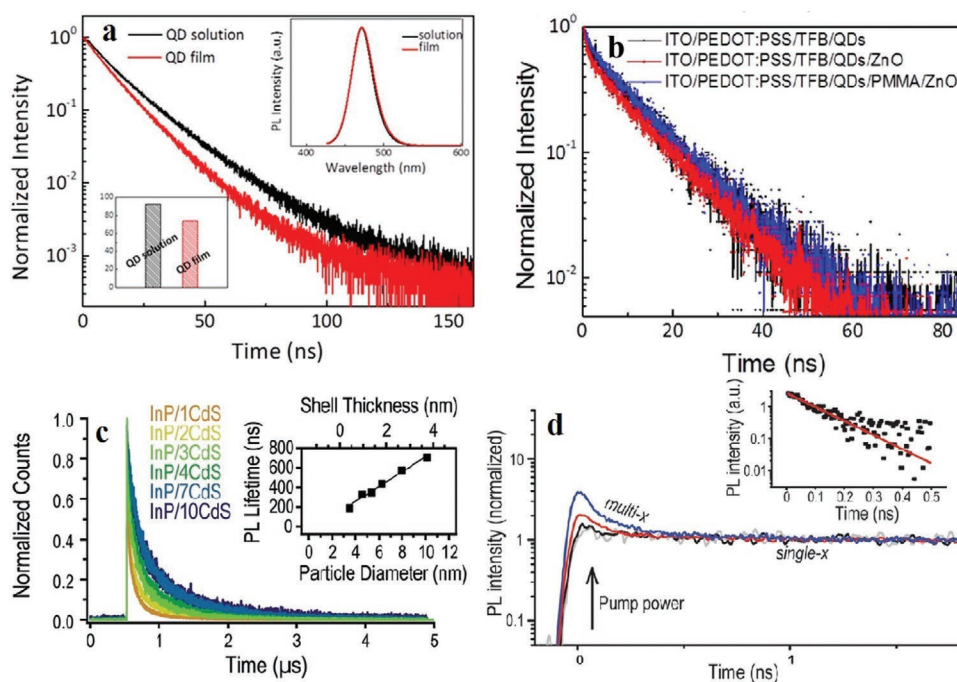


**Figure 5.** a) Transient PL spectra of ZnCdSe/ZnS//ZnS QDs in solution and solid film states. Insets show the normalized corresponding PL spectra and PLQY of QDs. b) PL lifetime of the ZnCdSe/ZnS//ZnS QD films contacting different layers. Reproduced with permission.<sup>[89]</sup> Copyright 2018, The American Chemical Society. c) PL decay curve from InP/CdS QD with varying shell thickness. Inset shows a plot of average lifetime versus shell thickness. d) Normalized pump intensity-dependent TRPL for InP/CdS QD showing the decay of multiexcitons. Extracted multiexciton decay component as well as a single exponential fit (red line) with a  $99 \pm 4$  ps biexciton decay as shown in the inset. Reproduced with permission.<sup>[93]</sup> Copyright 2012, The American Chemical Society.

of increasing shell thickness to inhibit FRET can be seen in Figure 5c. To reveal multiexciton decay dynamics, TRPL decay profiles are normalized at long delay times, and the low-pump intensity data are subtracted from higher-pump intensity profile. The corresponding power-dependent TRPL spectra are given in Figure 5d. Radiative biexciton lifetime is shorter than radiative single-exciton lifetime and the ratio between single exciton lifetime to biexciton lifetime is used as a parameter to evaluate the strength of the Auger combination.

Klimov and co-workers demonstrated TRPL as a tool to study the carrier multiplication (multiple exciton generations from a single-photon absorption event) in QDs. Carrier multiplication due to Auger decay of biexcitons is observed in CdSe QD by monitoring the PL decay curve obtained via TCSPC.<sup>[94]</sup> Single and multiexciton emission energies and decay dynamics of CdS/ZnSe core-shell QDs are monitored by TRPL to control the properties of type-II QDs with shell thickness.<sup>[95]</sup> Analysis of temperature-dependent PL decay curve using carrier trapping model gives information about energy and distribution of the surface-localized trap states.<sup>[96]</sup> TRPL also can be used effectively for real-time monitoring of QD-complex assembly formation. Composition of the assemblies and strength of electronic interactions between their components can be quantitatively characterized.<sup>[97]</sup> The PL decay dynamics can be altered as a result of passivation of nonradiative surface states or due to increasingly delocalization of electron and hole wave function as observed in type-II QDs. Achtstein et al. examined the carrier dynamics and exciton-phonon coupling in CdSe-CdS core-shell nanoplatelets with varying shell thickness by investigating the temperature-dependent TR and time-integrated data.<sup>[98]</sup>

## 2.2. Transient Absorption Spectroscopy

TAS measurements involve excitation of samples using a short-duration, usually, a femtosecond, duration optical pulse (the pump) and monitoring of the evolution of the excited population of charge carriers using a less powerful short pulse after a temporal delay (the probe).<sup>[31]</sup> Varying temporal delay between pump and probe allows recording all possible series of absorptions. The wavelength of the pump pulse is selected according to the electronic structure of QDs to promote exciton of interest and is possible to tune from the UV to the near-IR. The resulting absorption spectra give information about the dynamics of excited carriers being probed. The temporal resolution is determined only by the cross-correlation between the pump and probe pulses and carrier dynamics occurring on a ps timescales can be recorded via TAS. Another advantage is that the signal corresponding to the dark (nonemissive) states can also be detected.

During TA measurements, the photogenerated excitons make the transition to the ground state or surface states and TA signal from this excited QD is attributed mainly to two processes: state filling and carrier-induced Stark effect. In TA spectra, the negative absorption ( $\Delta A < 0$ ) is due to the bleaching of ground-state absorption, and positive absorption ( $\Delta A > 0$ ) is from photo-induced absorption (PIA) of the excited states and absorption photoproducts.<sup>[99,100]</sup> The bleach of ground-state absorption leads to distinct bleach band that can be assigned to  $1S$  ( $1S_e-1S_{3/2}$ ) transition,  $1P$  ( $1P_e-1P_{3/2}$ ) transition, etc.<sup>[84]</sup> The decay curves correspond to bleach, and PIA signal give insight into the relaxation process of excited QD. Ultrafast charge carrier dynamics studies in InP/ZnS QDs by TAS are given in Figure 6a–d.<sup>[101]</sup>

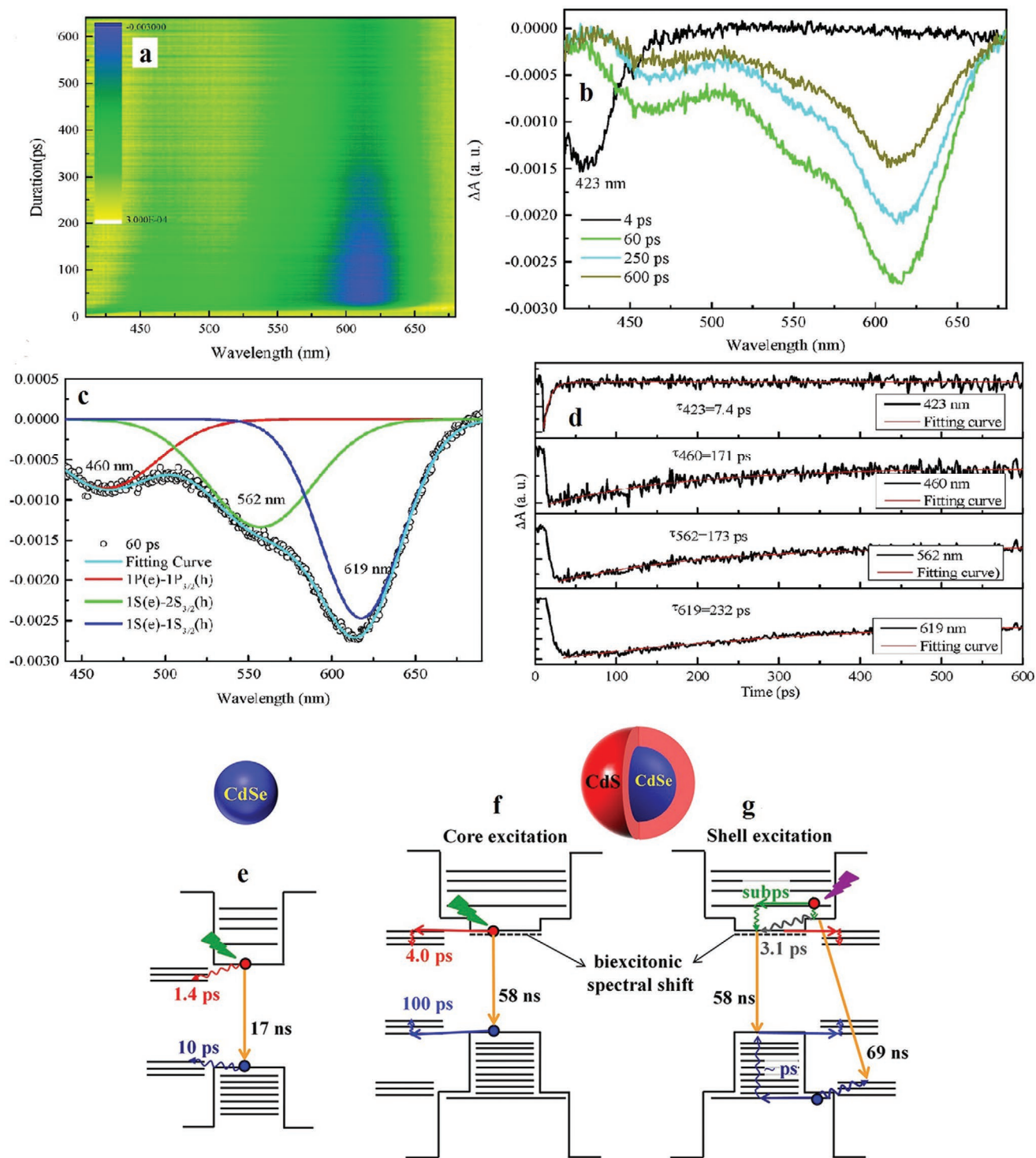


**Figure 6.** a) Transient absorption spectra of InP/ZnS QDs. b) TA at different delay times. c) Peak fitting and deconvolution of the TA for 60 ps delay time. d) PL lifetime fitting curves at 423, 460, 562, and 619 nm. Reproduced with permission.<sup>[10]</sup> Copyright 2019, The American Chemical Society. Carrier dynamics for e) CdSe core and f) for CdSe/CdS core/shell QDs with their 1S excitations. g) CdSe/CdS core/shell QDs with 400 nm excitation. Reproduced with permission.<sup>[11]</sup> Copyright 2018, The American Chemical Society.

The exciton dynamics in CdSe/ZnS QD, a type-I system, is thoroughly studied by various groups. It is reported that the negative signal in TA is from electron filling to the lowest

excitonic state (1S), and the positive signal in the visible region is due to biexcitonic-induced spectral shifts. The positive signal in the NIR region corresponds to trapped carrier-induced

absorption.<sup>[102–104]</sup> The intraband hot carrier relaxation process is investigated by TAS measurement in several QDs, including CdSe/ZnS, CdSe, CdTe, Te-doped CdSe, and many others.<sup>[105–107]</sup> As the trap states lie within the bandgap of QDs, charge carriers are trapped after photoexcitation. Usually, the process of trapping is speedy. Combined TRPL and TA studies in CdS QDs show that electron trapping is slower than hole trapping. The trapping times for electron and hole in CdS QDs are estimated to be 30 and 1 ps, respectively.<sup>[108,109]</sup> Van Patten and co-workers studied excited-state dynamics of charge carriers in CdTe nanocrystals and CdTe/CdS core-shell nanocrystals using pump-probe TAS, and the effectiveness of the passivating layer to quench the trapping is verified.<sup>[110]</sup> The dual-wavelength electroluminescence (EL) in CdSe/CdS tetrapods QDs is investigated using TR spectroscopy measurements. It is revealed that dual-wavelength EL can be achieved under relatively low electron-hole pair injection rates through a careful combination of nanoparticle structure and surface trap states.<sup>[111]</sup>

Depending on the density of trap states, interband electron-hole recombination also can occur during the relaxation process. Kambhampati carried out fs state-resolved pump-probe experiments on colloidal CdSe QDs to monitor the relaxation dynamics of hot excitons. Excitonic state-to-state transition rates are also quantified.<sup>[112]</sup> Interband recombination through phonon-assisted nonradiative interband relaxation is observed in CdSe QD. An Auger recombination-mediated relaxation process is observed in elongated CdSe nanocrystals (nanorods)

using TRPL and TA measurements.<sup>[113]</sup> Moreover, the correlation between the Auger recombination coefficient of the biexcitons and the average PL lifetime of single excitons is also observed. Lian and co-workers carried out TA studies and TRPL decay kinetics for CuInS<sub>2</sub> core and CuInS<sub>2</sub>/CdS core-shell QDs to investigate electron or hole dynamics separately and to estimate the lifetime of the single exciton.<sup>[114]</sup> Tamai and co-workers employed fs TAS to clarify the type-II band alignment in CdSe/CdS QDs, and the proposed carrier dynamics is given in Figure 6e–g.<sup>[115]</sup>

### 2.3. TR Spectroscopy Combined with SR Microscopy

Studies on blinking mechanism have assisted the exploration of energetic trap distributions and trap state lifetimes at individual QD level and are made possible by combining TR spectroscopic tool with SR microscopic tools.<sup>[39,116]</sup> For the blinking studies, single molecule is positioned with the help of a single-molecule confocal microscope, and TRPL signals are collected. The blinking is observed as ON and OFF states in the PL trace.<sup>[87,117,118]</sup> Photon-counting histograms correspond to each trace give a picture of ON and OFF states. A typical PL intensity trace is shown in Figure 7a–c in which the role of shell passivation in suppressing blinking can be clearly understood. The distributions of ON-times ( $P_{ON}$ ) and OFF-times ( $P_{OFF}$ ), ON-time fractions, and the average fluorescence intensity of the ON

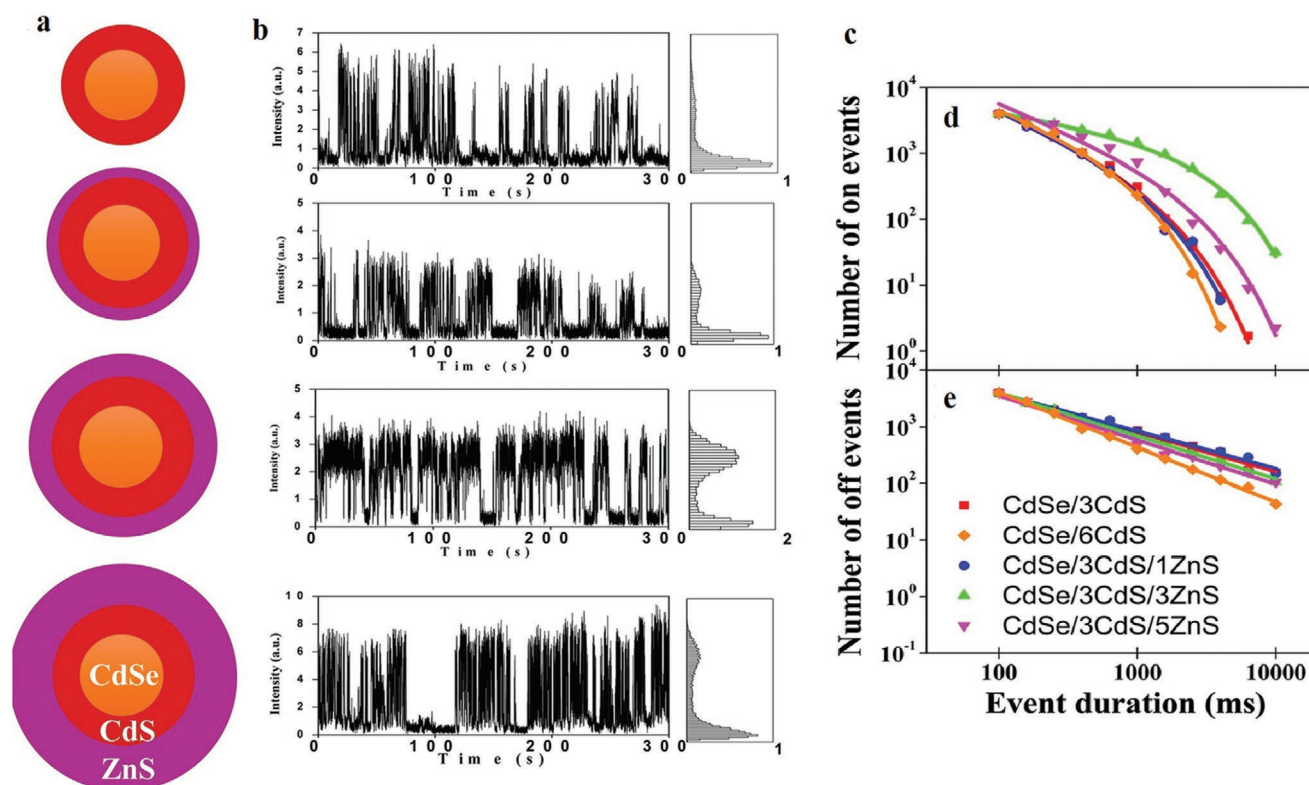


**Figure 7.** a) Schematic structures of CdSe/CdS/ZnS core/shell/shell QDs with ZnS outer shells thickness. b) Corresponding PL intensity traces, c) photon counting histograms, d) log–log plots of  $P_{ON}$ , and e) log–log plots of  $P_{OFF}$  distributions for CdSe/CdS (red, orange) and CdSe/CdS/ZnS (blue, green, and magenta) as a function of ZnS shell thickness under continuous-wave laser excitation. Reproduced with permission.<sup>[87]</sup> Copyright 2016, The American Chemical Society.

state from individual QDs can be extracted from the collected data. The behavior of ON and OFF states are obtained from log–log  $P_{\text{ON}}$  and  $P_{\text{OFF}}$  distributions. The log–log plot of  $P_{\text{ON}}$  and  $P_{\text{OFF}}$  corresponding to PL blinking in CdSe/CdS/ZnS system is shown in Figure 7d,e.

Kim and co-workers carried out blinking dynamics studies in CdSe/CdS QDs and InP/GaP QDs that investigate composition-dependent trap states present in core–shell structures.<sup>[119]</sup> The studies reveal the understanding of various radiative/nonradiative processes, as well as the Auger recombination rate, happened within the QDs. Htoon and co-workers combined single-nanocrystal spectroscopy with an electrochemical approach to investigate two distinct types of blinking mechanism (A-type and B-type) present in QDs.<sup>[120]</sup> Advantage of this approach is that the blinking processes can be controlled electrochemically through the application of proper potential. Fluorescence lifetime-intensity distribution (FLID) representation is a convenient tool to correlate the PL intensities and lifetimes. In FLID, the probability of the photon emission event is represented in a fluorescence lifetime-PL intensity plane as color code and as the probability density of the event increased the color gradually changes from blue to red. As compared to B-type blinking in which decrease in PL intensity occurs without effecting PL lifetime, in A-type blinking, decrease in PL intensity occurs simultaneously with shortening of the PL lifetime.<sup>[120]</sup> Hence A-type and B-type blinking can be easily differentiated in FLID and are given in Figure 8a,b. Statistical studies of the “ON” and “OFF” event durations also help differentiate between B-type and A-type blinking. Because, ON and OFF time durations for B-type follow a power-law distribution,

$P(t_{\text{ON/OFF}}) \approx (t_{\text{ON/OFF}})^{-\nu}$ , whereas for A-type blinking, the ON and OFF time distributions are fitted when introducing an exponential cutoff to the power-law distribution such that the distribution function is  $P(t_{\text{ON/OFF}}) \approx (t_{\text{ON/OFF}})^{-\nu} \exp(-t_{\text{ON/OFF}}/t_c)$ . The ON and OFF distribution corresponding to electrochemically controlled switching between B-type and A-type blinking in CdSe/CdS QDs is given in Figure 8c,d.

#### 2.4. SR Microscopy Combined with SR Spectroscopy

Scanning tunneling microscopy (STM) offers atomic-scale mapping of electronic states in individual QD.<sup>[66]</sup> In STM, a sharp metallic tip typically made of platinum–iridium (Pt–Ir) or tungsten is brought into very close proximity ( $\approx 3\text{--}10 \text{ \AA}$ ) to a conducting or semiconducting surface. The STM measures the tunneling current produced due to the quantum tunneling of electrons between the tip and the surface. Advantage of STM over other optical spectroscopy techniques is that they are not subjected to quantum selection rule.<sup>[121,122]</sup> In STM, the energy levels in valence and CBs are probed individually, which is limited in an optical spectroscopic technique. Observation of allowed transitions between valence and conduction energy levels is only possible with optical spectroscopies. Though STM offers feasible imaging at atomic and molecular resolution, the topographic STM images can contain information about both geometric surface structure and local density of electronic states (LDOS) of the tip and the sample surface. To separate LDOS information from the sample surface, scanning tunneling spectroscopic (STS) technique is

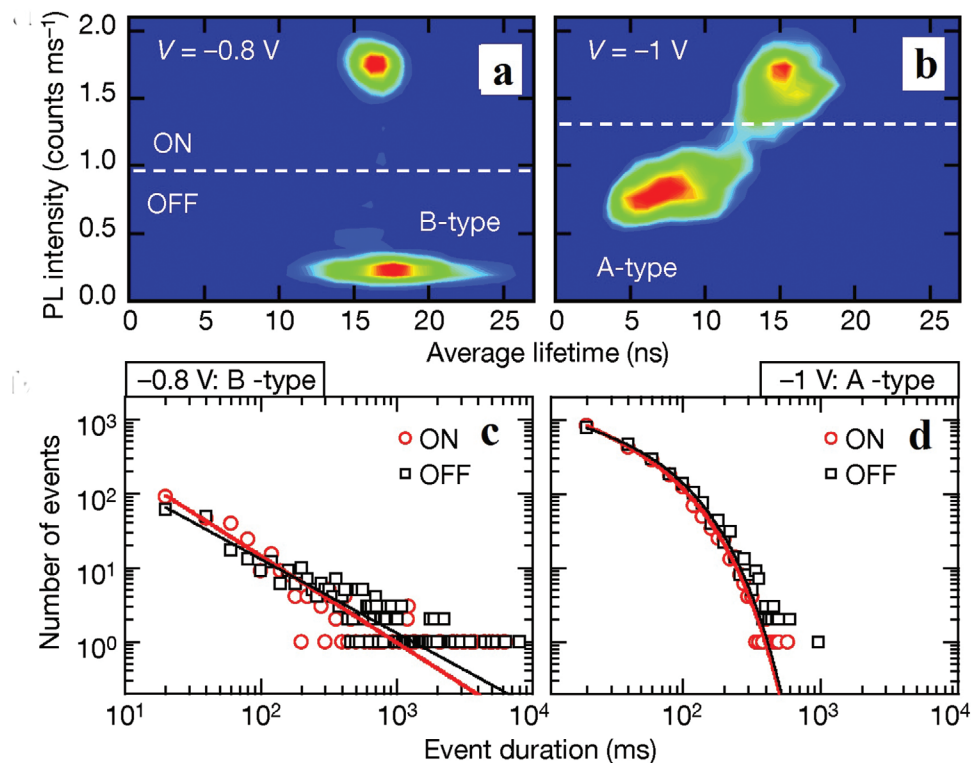


**Figure 8.** FLID shows the switching from B-type to A-type blinking at electrochemical potential a,b) 20.8 and 21 V, respectively, and c,d) the corresponding ON and OFF time statistics. Reproduced with permission.<sup>[120]</sup> Copyright 2011, Nature.

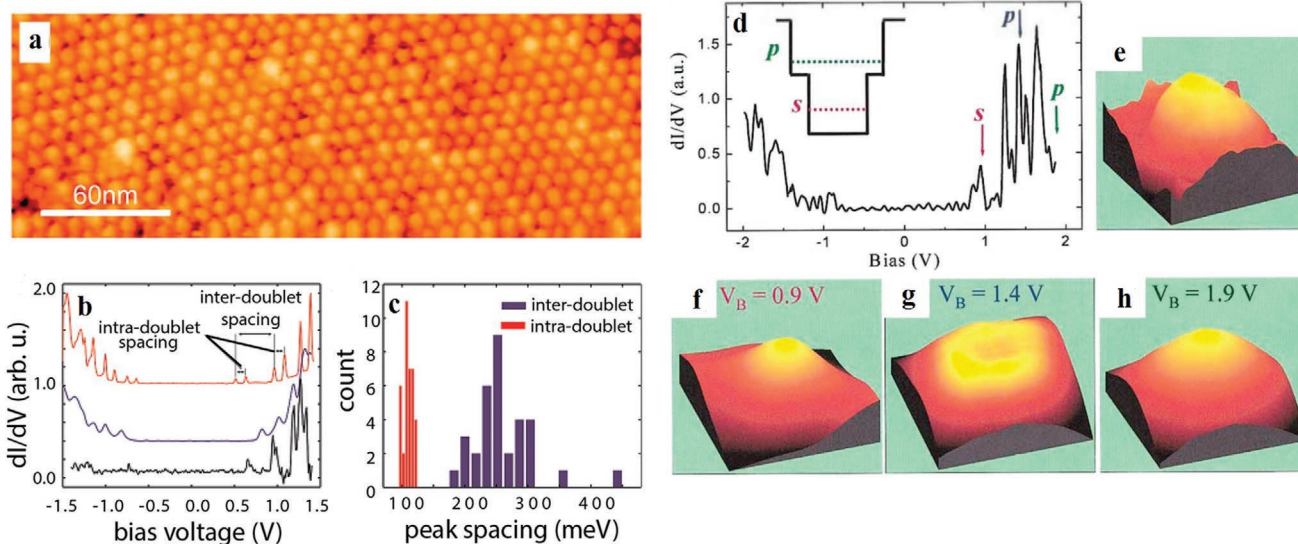


**Figure 9.** a) Low-temperature STM topographic image of PbSe/CdSe QDs on HOPG. b) Low-temperature  $dI/dV$  spectra over PbSe/CdSe core-shell QD (red), its core PbSe (blue), and its shell CdSe (black). c) Histograms of intra-doublet spacing and inter-doublet spacing measured from the  $dI/dV$  spectrum. d) STS spectrum over a single InAs/ZnSe core-shell QD. e) Its STM topographic image (f–h) tunneling current images at different biases. Reproduced with permission.<sup>[66]</sup> Copyright 2015, The American Chemical Society.

performed in which the tip is scanned over the surface feature at a fixed sample height. By measuring the tunneling current ( $I$ ) as a function of bias voltage ( $V$ ), the LDOS information can be obtained. In addition to  $I/V$ , first derivative tunneling current termed as differential conductance can also be recorded in STS that resolve various electronic energy-level positions. STS has been employed to obtain quantitative information on the energy levels and the Coulomb interactions of semiconductor QDs. STS technique accesses all the energy states and probes the LDOS even in single QD. Spatial localization and spectral properties of sub-bandgap states in QDs can be investigated by STS-based mapping of LDOS.<sup>[123]</sup>

In STM, a double-barrier tunnel junction geometry can also be used to measure tunneling rates of electrons/holes in isolated QDs. The electron (hole) states appear as peaks in STS spectra at positive (or negative) bias.<sup>[124]</sup> With the help of STS spectra, it is accessible to distinguish the electronic structure of QDs from their respective cores and shells. STM topographic image of PbSe/CdSe QDs on highly oriented pyrolytic graphite (HOPG) is shown in Figure 9a. From the low-temperature  $dI/dV$  spectra (Figure 9b) of core-shell PbSe/CdSe (red), core PbSe, and shell CdSe (black), it can be observed that multiple doublets with unique characteristics have appeared for core-shell structures. At the same time, they are absent for their respective core and shell. Electronic energy gaps can be calculated from the spectra with high accuracy. Histogram of energy gap measured from the STS spectra is given in Figure 9c. The spacing within each doublet gives intra-doublet spacing, and that between each pair of doublets gives inter-doublet spacing. Banin and co-workers carried out STS analysis on InAs/ZnSe QD with different shell thicknesses, and the studies provide insight into overlapping and intermixing of energy states at the core-shell interface during the shell growth.<sup>[125]</sup> Spatial distribution of electron/hole states can be imaged via STS. The spatial mapping of energy

levels in InAs/ZnSe core-shell QDs by STS is well described in the previous works, and the corresponding images are given in Figure 9d–h.<sup>[66]</sup>

Surface states in individual QDs can be investigated in real space by combining STM and STS. The surface reconstructions from STS mapping lead to the appearance of ordered atomic planes in crystalline QDs. Nazin and co-workers reported for the first time the connection between the atomic-scale nanocrystal surface morphology and atomic-scale variations in the electronic DOS.<sup>[126]</sup> Figure 10 exhibits the reported crystallographic directions and nanocrystal boundaries to identify via STS DOS mapping. The spatial mapping allows identifying the delocalized quantum-confined states and localized sub-bandgap states in PbS nanocrystals. Surface-bound sub-bandgap electronic states with spectral and spatial properties sensitive to the local stoichiometry of nanocrystal surfaces are observed in the reconstructed surface images.<sup>[127]</sup>

### 3. SR and TR Tools for Morphological, Structural, Compositional, and Electrical Characterization of QDs

With the ability to control the parameters such as composition, uniform doping, size, and strain distribution in the QDs, the crystalline structure at the QDs core-shell interface and tuning work function of QD are crucial for the development of QD with promising device application. Hence, attempt to improve the device performance include quantitative measurement of all the fundamental properties including, size, crystalline structure, work function, strain distribution, etc., and is now possible with the help of SR microscopic and spectroscopic tools and TR microscopic techniques.

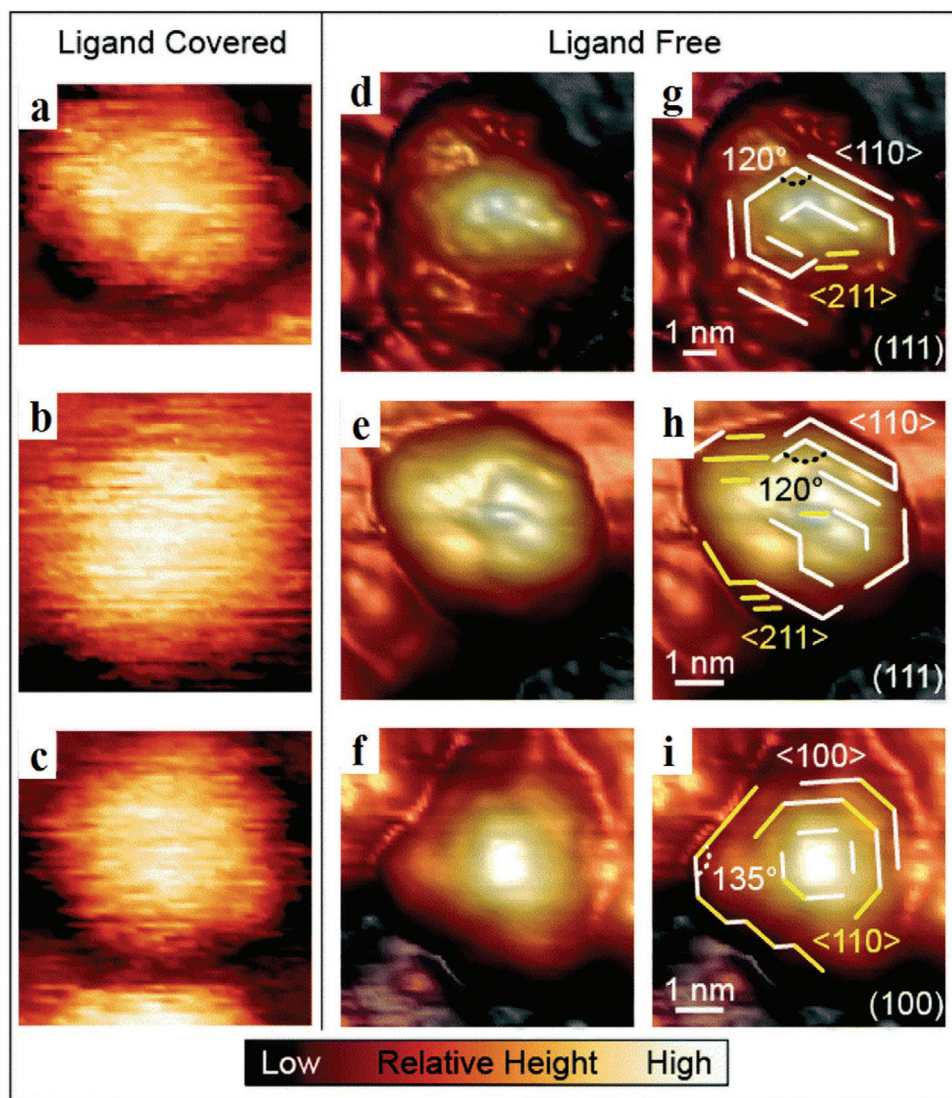


**Figure 10.** STM topographies of a–c) ligand-covered and d–f) ligand-free PbS NCs. The topographical features highlighted in (g–i) highlight crystalline directions of topographic features observed in (d–f). Reproduced with permission.<sup>[127]</sup> Copyright 2015, The Royal Society of Chemistry.

### 3.1. SR Microscopy for Structural, Morphological, Compositional, and Electrical Characterization

Electron microscopy-related techniques such as transmission electron microscopic (TEM) imaging, high-resolution TEM (HRTEM) imaging, selected area electron diffraction (SAED), energy-dispersive X-ray spectroscopy (EDX), and electron energy loss spectroscopy (EELS) have been efficiently exploited as powerful tools to image morphology and crystal structures of QDs directly and to map the chemical elements in the QDs.<sup>[128–130]</sup> TEM allows direct visualization of real space of the sample and hence capable of measuring QD size and its size distribution accurately. The internal structure of the QD core can be investigated by HRTEM.<sup>[131,132]</sup> It is difficult to discriminate the core–shell interface from HRTEM images if the electron scattering cross-sections of core and shell are almost the same. When individual QD is examined by TEM, other than average crystal size, it provides much more information such as particle size, shape, crystal orientation, defects, and

surface structures.<sup>[133–135]</sup> Different lattice planes can be seen in HRTEM images, and the corresponding inter planar spacing (d-spacing) calculations allow to determine specific crystal orientation in the sample area selected for imaging. However, the accurate calculation of d-spacing from HRTEM images is difficult, and it is a challenging task to obtain information from all lattice planes present in the QD. Sample damages during measurement can be reduced with the advent of scanning TEM (STEM) technique. The particle size measurement from STEM results well agrees with HRTEM results. Selected area diffraction studies can image diffraction signals collected from all the crystal planes, and the corresponding SAED pattern appeared as annular rings. The potential of electron microscopic techniques for morphological and crystalline characterizations of QDs is clearly understood from the data provided in **Figure 11**.

Chemical composition of individual QD can be examined by EDX analysis in which X-rays are emitted from the specimen upon interaction with the e-beam. Variation of chemical composition in the sample can be obtained from EDX point analysis, and

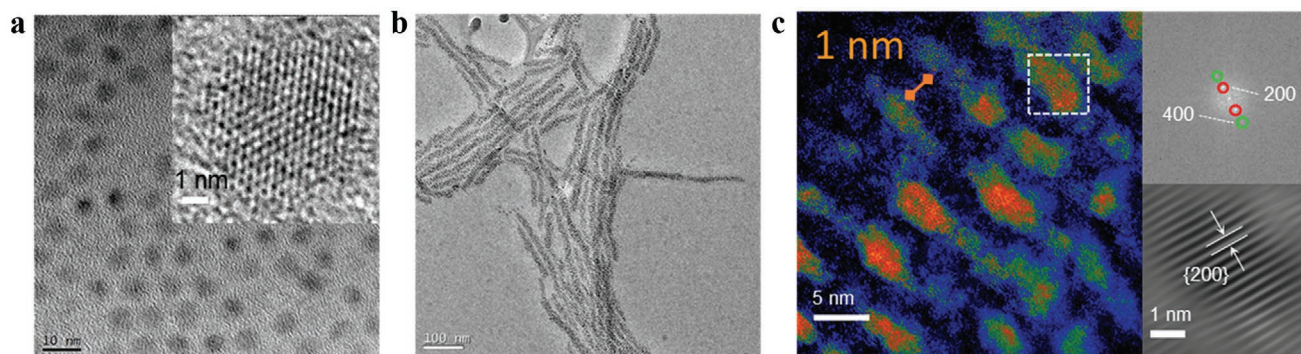


**Figure 11.** a) TEM images of PbS QDs. Scale bar = 10 nm. Inset is the HRTEM image taken from [001] zone axis. Scale bar = 1 nm. b,c) HAADF-STEM false color-scale images of the QDs. The insets of (c) are the fast Fourier transform nanopattern (top) and enlarged STEM image (bottom). Reproduced with permission.<sup>[133]</sup> Copyright 2019, Elsevier.

the EDX mapping helps to provide the elemental distribution in the QDs. Since the EDX signal from the specimen is affected by many factors including sample thickness, the energy of e-beam, and selected sample area and its surrounding environment, the accurate determination of chemical composition by EDX is a challenging task. Additionally, the probability of error during quantification is high as a result of the overlap of peaks from different elements. Elemental mapping is also possible by EELS in which variations in kinetic energy of electrons after interacting with the specimen are collected. EELS allows determining type, quantity, and the chemical state of atoms to investigate the collective interactions of the atoms with their neighbors.<sup>[136]</sup> The elemental mapping of CdSe QD by EELS is shown in **Figure 12**. The information gathered through EELS is somewhat similar to EDX, but both have its own merits and demerits.<sup>[137]</sup> EELS is identified as much more sensitive technique for light elements whereas EDS for heavy elements. Though EDX is easy to use, the spatial and energy resolution is high for EELS as compared with EDX.

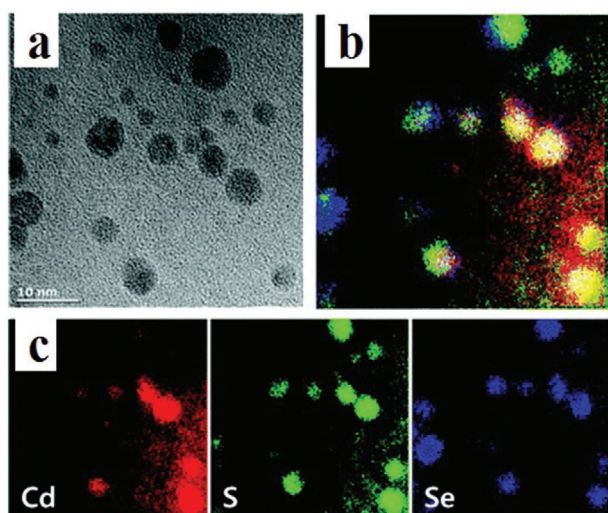


**Figure 12.** a) TEM image of CdSe QD for EELS analysis. b) Combined EELS image of the constituent elements Cd, S, and Se. c) EELS elemental mapping of Cd, S, and Se. Reproduced with permission.<sup>[136]</sup> Copyright 2016, The Royal Society of Chemistry.

Accurate size and concentration determination of QD is possible by small-angle X-ray scattering (SAXS) in which spatially localized measurements are created using an X-ray beam either focused or confined laterally to the beam propagation.<sup>[138]</sup> The beam size and scanning precision control the spatial resolution of the image and the real space image of the sample volume can be produced via SAXS. As compared to TEM, SAXS allows measurement on QDs not only in solution and but also ensemble films with  $\approx 10^9$  QDs can be analyzed during one measurement. The self-assembly of colloidal semiconductor nanocrystals is one of the synthetic strategies used to pack the nanocrystals into superlattices that offer minimum average interparticle distance, and hence improve the device performance.<sup>[131]</sup> Therefore, characterization of superlattices in QD monolayers, especially information on morphology and interparticle distance, is significant, and grazing-incidence small-angle X-ray scattering (GISAXS) has emerged as a versatile and detailed characterization technique for understanding superlattice of QD monolayers. GISAXS can extract morphological information from QD monolayer surface and also from the buried structures. It reveals information on the size/shape of nanostructure and how they arrange over the surface. Tisdale and co-workers employed GISAXS to study the effect of ligand length in the self-assembly of colloidal PbS nanocrystals into superlattice structures and to evaluate the packing efficiency of PbS QD monolayer.<sup>[139]</sup> GISAXS patterns for PbS nanocrystals having oleic acid, dodecanoic acid, and hexanoic acid as surface ligands are shown in **Figure 13a–c**. The superlattice of monolayer depends on the surface ligand length and is visible in the pattern. From the GISAXS pattern shown in **Figure 13d,e**, size dispersivity of PbS monolayer is investigated. It is observed that all individual QDs are oriented in the same way with the atomic planes aligned in PbS monolayer with dispersivity ( $\delta$ ) < 3.4% and hence the solid shows a highly ordered superlattice. In contrast, the monolayer with  $\delta$  < 4.9% is less ordered. Recently, X-ray absorption fine structure spectroscopy (XAFS) is used to reveal detailed information about local atomic arrangements and chemical composition of compounds in vivo at high spatial resolution.<sup>[140]</sup> In QD research, it is mainly employed for the characterization of biogenic QDs (bio-QDs).<sup>[141,142]</sup> The biotransformation of  $\text{CdS}_x\text{Se}_{1-x}$  QDs in *Escherichia coli* is validated by examining their species in vivo XAFS.<sup>[143]</sup> Wang and co-workers

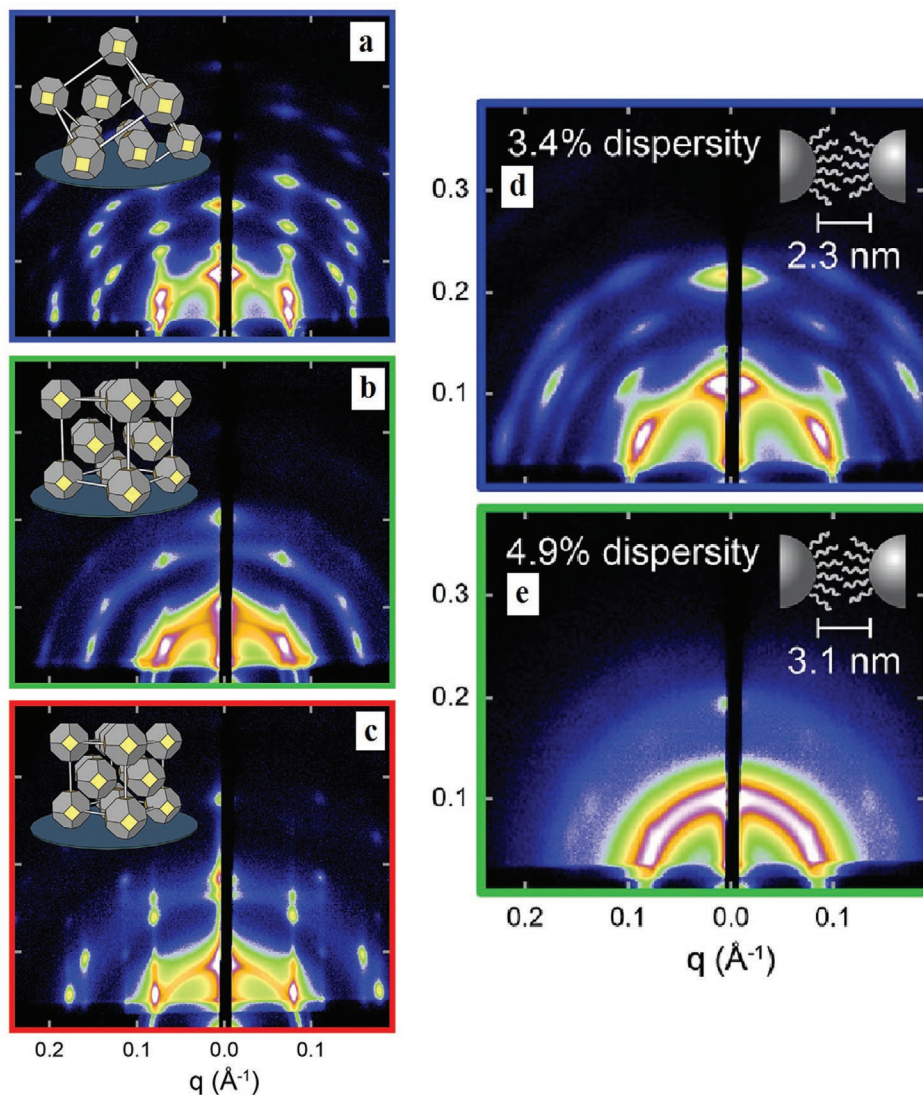


**Figure 13.** a–c) GISAXS pattern for PbS QDs with surface ligands oleic acid, dodecanoic acid, and hexanoic acid and d,e) GISAXS patterns for PbS with  $\delta < 3.5\%$  and  $\delta < 4.9\%$ . Reproduced with permission.<sup>[139]</sup> Copyright 2018, The American Chemical Society.

employed XAFS as a tool to examine the chemical stability of Ag<sub>2</sub>S QDs in human mesenchymal stem cells.<sup>[144]</sup>

Atomic force microscopy (AFM) is a potential tool to visualize the morphology of QDs. In AFM, tip–sample interaction forces are recorded using a force-sensing cantilever to measure the surface properties of the specimen at high spatial resolution. The key

advantages of AFM over TEM include the capability to image 3D features, and scanning over a large area in lesser time, vacuum-free, and little specimen preparation. AFM images in **Figure 14a,b** show the morphology of CdTe QD synthesized for different reaction conditions as prescribed in the report by Poderys et al.<sup>[145]</sup> Mishra et al. carried out AFM measurement on PbSe/PbS

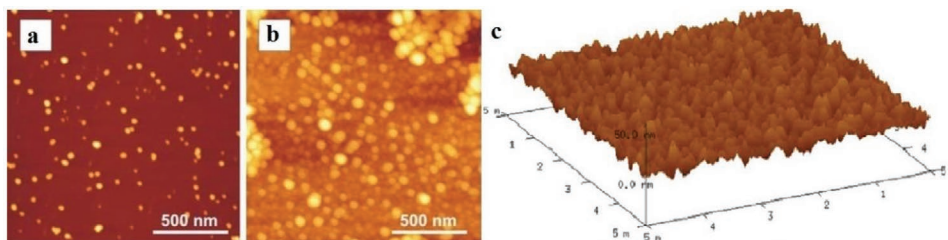


**Figure 14.** a,b) AFM images of CdTe QDs dispersed on mica at different experimental conditions. Reproduced with permission.<sup>[145]</sup> Copyright 2010, BioMed Central. c) AFM image of PbSe/PbS tetrapods film onto a glass substrate. Reproduced with permission.<sup>[29]</sup> Copyright 2016, The Royal Society of Chemistry.

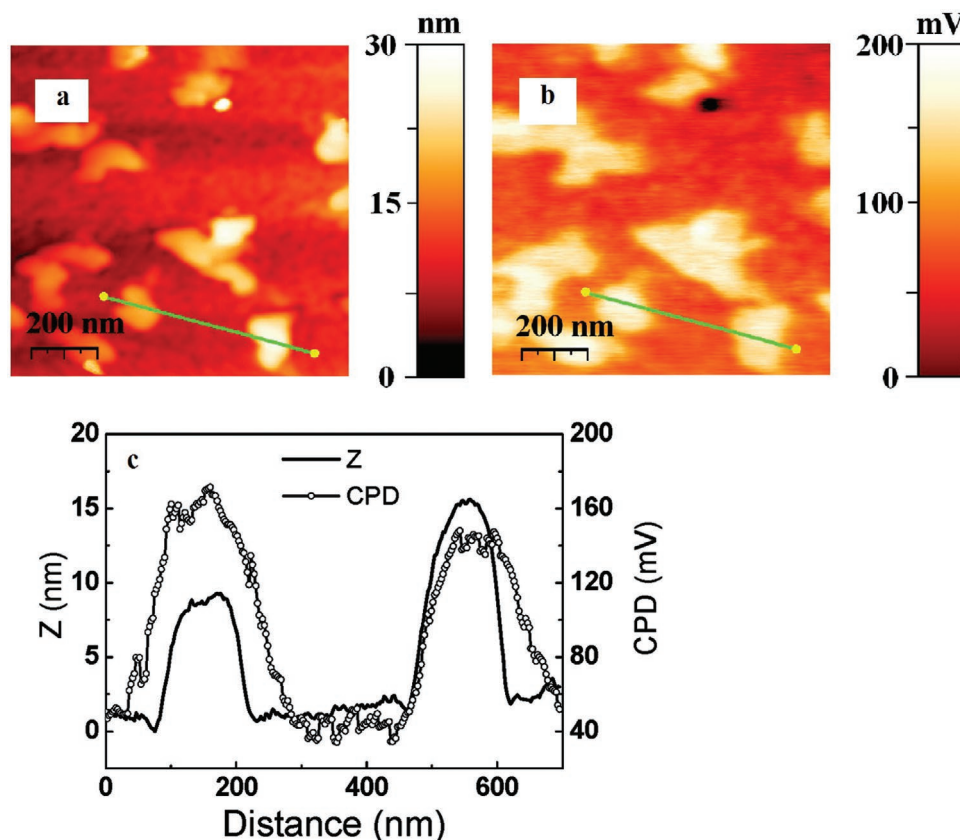


**Figure 15.** a) Topography and b) CPD image of InSb nanocrystals grown on GaSb substrate. c) The line profiles along the green lines on the corresponding images (a) and (b). Reproduced with permission.<sup>[149]</sup> Copyright 2007, The American Chemical Society.

tetrapods film in the active area of photodetector. They verified that the film is smooth and uniform (Figure 14c).<sup>[29]</sup> Nevertheless, the accuracy of AFM data heavily depends on the dimension and quality of AFM tips and the sample–tip interaction.

Kelvin probe force microscopy (KPFM) and electric force microscopy (EFM) are advanced AFM techniques used to probe nanoscale electrical properties of QDs. Here, the AFM probes are coated with a conducting material, typically Pt/Ir, and the electrostatic forces between the probe tip and the sample are recorded. The difference in the work function of the tip and the sample generates a contact potential difference (CPD) and hence an electrostatic force that induces cantilever oscillations. The changes in frequency/amplitude or phase of these oscillations are detected, and potential images are generated. Variations in CPD over the surface are recorded during KPFM measurements. KPFM is identified as a noninvasive technique to measure relative work function between a reference probe and the sample under vacuum or ambient operating conditions with a nanometer-scale resolution.  $V_{\text{CPD}}$  is defined as the difference in work function ( $\Phi$ ) between sample and tip, where  $e$  is the elementary charge

$$V_{\text{CPD}} = (\Phi_{\text{sample}} - \Phi_{\text{tip}}) / e \quad (6)$$

Using a calibrated tip, Equation (6) can be used to deduce the work function of the sample at an absolute scale. Usually, a gold electrode is employed as tip and HOPG is used for calibration. Kulis et al. measured the working function of various nanocrystals

such as PbS, ZnO, CdS, and  $\text{Cu}_2\text{S}$  by KPFM.<sup>[146]</sup> Yamauchi et al. investigated the size-dependent work function in InAs QDs on GaAs(001).<sup>[147]</sup> In their studies, simultaneous measurement of topographic and CPD images was carried out to investigate the correlation between size and local work function of QDs. Nanometer-scale work function measurements using ultrahigh vacuum KPFM help to investigate the strain and composition variations within and around the individual QDs.<sup>[148]</sup> The topographic and CPD images recorded for InSb nanocrystals grown on GaSb substrate by KPFM are presented in Figure 15a,b. The corresponding profile to measure the work function is also given as Figure 15c.

In EFM, changes in electrostatic force over distance are recorded through the changes in the phase of cantilever oscillations. EFM possess higher spatial resolution than KPFM, but direct measurement of surface potential is not possible in EFM. Usually, EFM measurement is carried out in QD samples for determining its charge states under the influence of illumination or the underlying substrate. Ben-Porat et al. demonstrated the role of n-type/p-type substrate and light illumination in determining the charge state of the QD layer through EFM analysis, and the results are shown in Figure 16.<sup>[148]</sup>

### 3.2. SR Spectroscopy for Structural Characterization

Understanding of the core–shell structure and its interface is essential for the synthesis of core–shell QDs with efficient

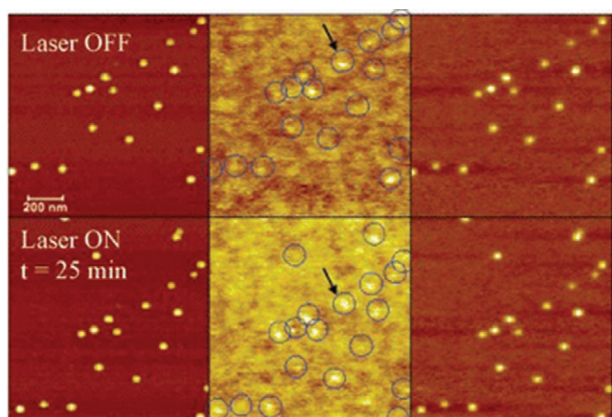


**Figure 16.** Top row EFM images correspond to the topographic (left), charge (middle), and polarizability (right) images of PbSe QDs on an n-type silicon substrate under dark conditions and bottom row images correspond to that of under illumination. Reproduced with permission.<sup>[66]</sup> Copyright 2015, The American Chemical Society.

emission properties. Raman spectroscopy has been demonstrated as a potential tool to investigate the structure of mono- and sub-monolayer shells and the interface in core-shell QDs. Compound alloying is one of the methods to enhance the quantum yield of QDs and Raman spectroscopy is particularly used to confirm the formation of alloy at the interface.<sup>[150,151]</sup> Compositional intermixing at the core-shell interface can be deduced by analyzing Raman peaks due to optical phonons inside the core and those related to the core-shell.<sup>[152]</sup> Dzhagan et al. observed a shift in the Raman-active longitudinal optical (LO) phonon in CdSe QD, which is attributed to phonon confinement and strain effect during the nanocrystal growth.<sup>[153]</sup> Significant changes such as the appearance of new Raman peaks and increased FWHM of Raman peaks were also noticed upon the passivation of shell around CdSe core.<sup>[154–156]</sup> On a comparative analysis of optical and vibrational spectra, it can be possible to derive a dependence of core-shell structure on the synthesis method of the shell. As shown in **Figure 17**, it is possible to resolve the respective contributions from core, shell, and the alloyed interface from Raman spectra. Dzhagan et al. studied the effect of the shell thickness on vibrational resonance Raman spectra of CdSe/ZnS QD, and a decrease in 2LO/LO intensity ratio of the CdSe phonons due to the weakening of exciton coupling to the phonon upon ZnS shell deposition.<sup>[153]</sup> The average composition of alloy interface and the strain evolution in core-shell can be investigated by combined analysis of Raman and IR spectroscopy.

### 3.3. TR Microscopy for Tracking the Evolution of QD Formation

As the QDs with unique optical and electrical properties can be synthesized by empirically changing the experimental reaction conditions, a methodology to investigate the fundamental QD formation mechanism would accelerate the development process of QDs with precisely tailored properties.<sup>[157]</sup> As high-energy synchrotron X-rays can efficiently penetrate through liquid media, they are an excellent probe for in situ monitoring

of nanoparticle growth in liquid media. The TR synchrotron X-ray-based techniques include SAXS and wide-angle X-ray scattering (WAXS).<sup>[60]</sup> SAXS offer the simultaneous monitoring of concentration or mass and size of nanoparticles as a function of time. The information about precise crystallographic phases of nanoparticles with sizes >5 nm during nanoparticles growth can be probed through TR WAXS.<sup>[158]</sup> Abécassis et al. employed TR SAXS/WAXS to get a complete movie of CdSe QD formation from the self-assembly of their corresponding precursors.<sup>[68]</sup> For instance, in situ SAXS measurements were carried out to monitor the growth of CdSe QDs (**Figure 18**). As shown in Figure 18, during the heating process, first CdSe QD ( $t = 0$ ) was formed at 218.7 °C. Subsequent SAXS/WAXS measurements are carried out that probed the appearance of (220) peak during QD formation.

Knowledge of thermal and temporal behavior of QDs has crucial importance for its implementation in optoelectronic devices. Heating of QD causes segregation of its components that eventually alters the performance of QDs. *ChemTEM* is an emerging advanced transmission microscopic (TEM) tool that allows studying chemical reaction under e-beam.<sup>[159]</sup> In *chemTEM*, e-beam transfers its energy directly to the molecule that enables in situ investigation of a chemical reaction. The final product formed during the *chemTEM* process is determined by the nature of both e-beam and the reactant molecule, while the e-beam dose controls the rate of chemical reactions. Thermally induced structural and morphological changes of CdSe/CdS octapods were examined by coupling in situ TEM with MEMS technology.<sup>[160]</sup> Yalcin et al. also followed the same methodology to investigate the thermal evolution of CdSe/CdS/ZnS core-multishell QDs.<sup>[161]</sup> The high-angle annular dark-field STEM images (HAADF-STEM) and EDX elemental mapping in **Figure 19** show the thermal evolution of CdSe/CdS/ZnS QDs to  $\text{Cd}_x\text{Zn}_{1-x}\text{Se}/\text{Cd}_y\text{Zn}_{1-y}\text{S}$  QDs at 275 °C.

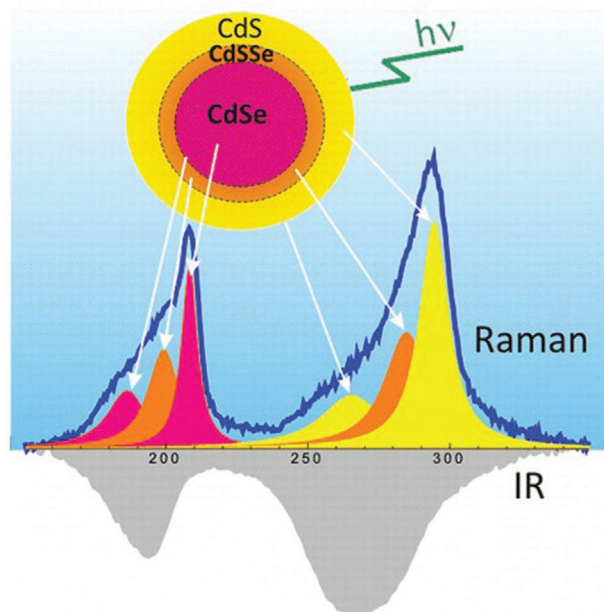


**Figure 17.** IR and Raman spectrum of CdSe/CdS core-shell QDs. Reproduced with permission.<sup>[150]</sup> Copyright 2013, The American Chemical Society.

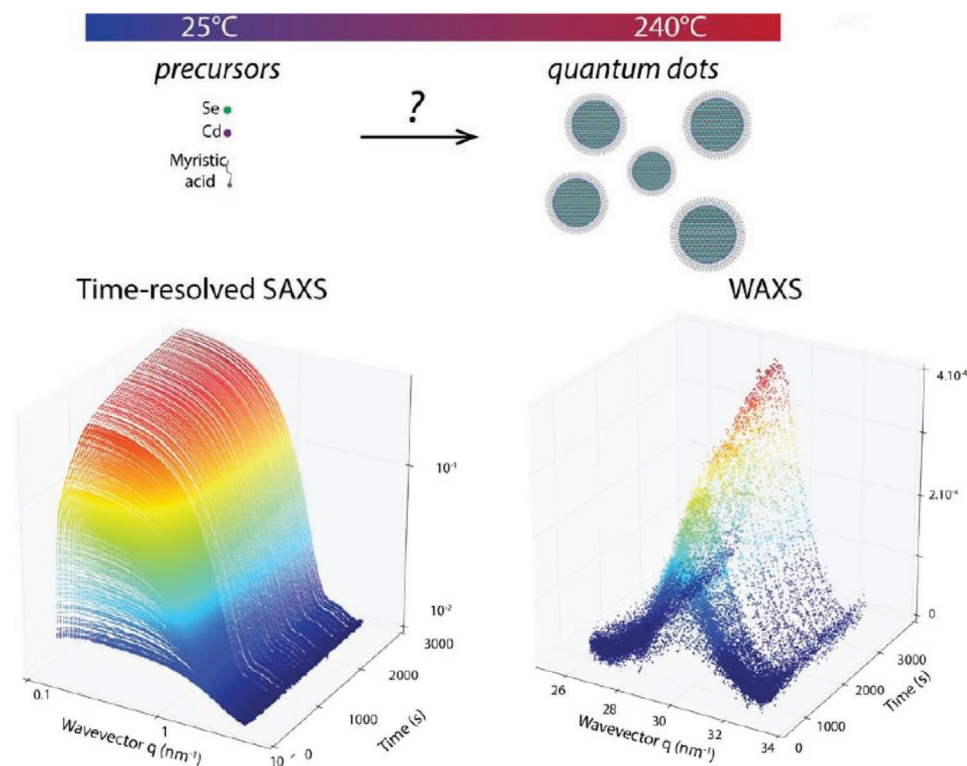


**Figure 18.** Time series of SAXS (left) and WAXS (right) patterns recorded during the formation of the QDs. The intensity increases as color code goes from blue to red. Reproduced with permission.<sup>[68]</sup> Copyright 2015, The American Chemical Society.

#### 4. Challenges and Future Developments of TR- and SR-Based QD Metrology

Recent progress in the TR and SR analysis of QDs has provided a new understanding of the role of size, morphology, core-shell interface, composition, and shell thickness in QD optoelectronic device performances. Various TR and SR tools discussed in this work for QD microstructural metrology have been summarized in **Table 1**. It can be seen that most of the

analytical technique is operated in high-vacuum condition, which is expensive and time-consuming. The data collection is a tedious task in various characterization techniques, including XPS, TEM, and STM, due to the failure of inappropriate sample preparation. Application of established analytical probes is also limited for in situ analysis of QD. These limitations promote the development of TEM analysis in liquid, environmental STM and XPS, etc. Cryogenic TEM (cryo-TEM) provides the opportunity to analyze liquid samples and helps to track the evolution

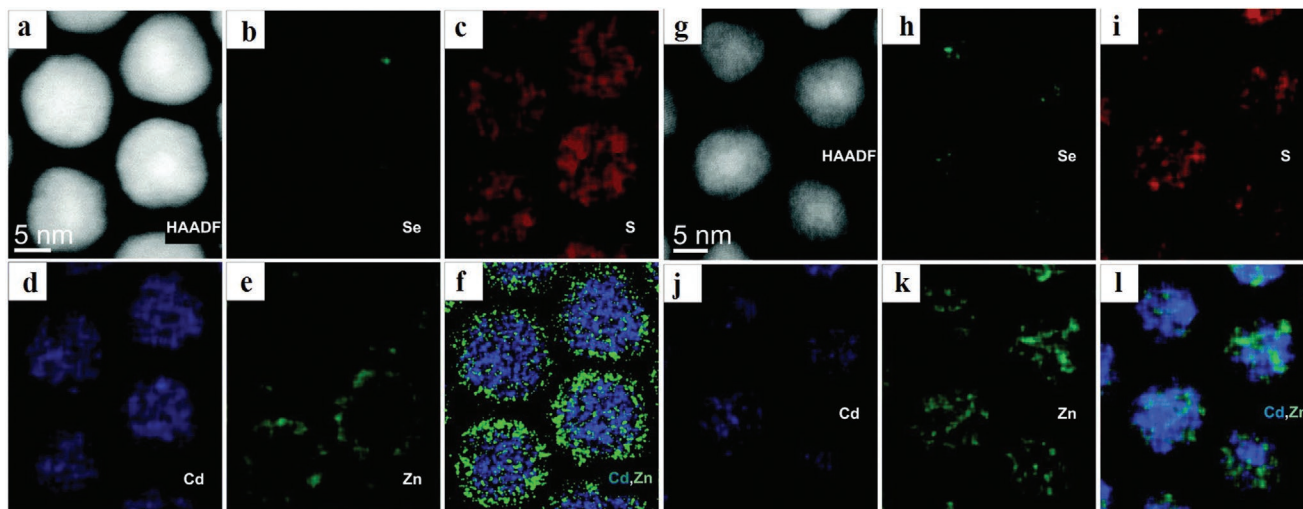


**Figure 19.** HAADF-STEM image and EDX mapping of CdSe-CdS-ZnS core-multishell QDs at a-f) RT and g-l) 275 °C. Reproduced with permission.<sup>[161]</sup> Copyright 2015, The Royal Society of Chemistry.

**Table 1.** Summary of SR and TR tools for QD microstructural metrology.

Property	Tool	Reference
Morphology	HRTEM, STEM, AFM	[131,145]
Self-assembly of QDs and concentration of QD and its film	SAXS	[138]
Superlattices in QD monolayers	GISAXS	[139]
Structure	SAED	[133,134]
Composition	EDX, EELS	[136,137]
Composition of bio-QDs	XAFS	[143,144]
Composition at core–shell interface	Raman mapping	[152,153]
Average PL lifetime	TRPL	[93]
Carrier multiplication	TRPL	[94]
Biexciton lifetime	Pump power-dependent TRPL	[93]
FRET probability	TRPL	[90]
Electron and hole trapping	TAS	[108,109]
Relaxation dynamics of hot excitons	TAS	[105–107]
Type-II band alignment	TAS	[115]
Energetic trap distributions and trap state lifetimes/blinking	Single-molecule confocal microscope and TRPL	[117,118]
Atomic-scale mapping of electronic states	STM	[66]
LDOS	STS	[123]
Electronic energy gaps	STS	[124]
Intra-doublet spacing and inter-doublet spacing	STS	[124]
Spatial distribution of electron/hole states	STS	[125]
Energy states at core–shell interface	STS	[125]
Work function	KPFM	[146,147]
The charged state of QD	EFM	[149]
In situ monitoring of QD growth	TR WAXS/SAXS	[68,158]

of inorganic nucleation and growth in solution with nanometer spatial resolution and a temporal resolution of  $<1$  s.<sup>[162,163]</sup>

A thorough understanding of the electronic coupling between QDs and the substrate material is required to design QDs effectively.<sup>[164]</sup> The electron coupling between QDs depends on the overlap between exciton wave functions. Researchers have used indirect methods such as TAS to study this overlap wave function and “evanescent electron wave function.”<sup>[165]</sup> TR photoelectron spectroscopy (TRPES) is an emerging tool that helps to study “evanescent electron wave function” and electronic structure dynamics in which photoelectron spectroscopy is combined with a pulsed laser.<sup>[166]</sup> In TRPES, the sample is excited with a pump of visible or near-IR light and X-ray radiation is used to emit electrons from the sample, and TRPES technique is applied in the gas phase of CdSe nanocrystals to directly measure evanescent electron wave function.<sup>[167]</sup>

A fundamental insight into controlling growth processes will eventually allow us to design efficient core–shell QDs with pre-determined and potentially unique properties. A deeper understanding of the growth mechanism is possible by combining

cryo-TEM with complementary techniques such as liquid-phase AFM, Raman spectroscopy, SAXS/WAXS, and computer simulations. Continuous improvement in spatial and temporal resolution is essential to fulfil the challenge of TR X-ray microscopy, and it is driven by both modification in X-ray source properties and end-station instrumentation. TR X-ray microscopy generates multidimensional data corresponding to 3D real space, 3D reciprocal space, and multidimensional spectra, and the analysis of these data awakes the necessity of progress in the computer vision and image reconstruction.<sup>[168,169]</sup>

Single-molecule absorption-scanning tunneling microscopy (SMA-STM) is an emerging tool to image the electronic excited states at different orientation that could give a better 3D structure view of the excited states.<sup>[170]</sup> The SMA-STM is advancing towards the possibility of single-particle tomography of excited states that could highlight the defects rather than an average structure obtained via cryo-TEM. Smaller and faster are vital concepts underlying the progress of both SR and TR tools. A new methodology, combining STM with optical pump-probe technique, enables visualization of transient charge carrier dynamics with an STM spatial resolution.<sup>[171]</sup> Real-time observation of chemical reactions and dynamic motion of single molecules is made possible with single-molecule atomic-resolution real-time (SMART) TEM imaging technique.<sup>[172]</sup> SMART-TEM opened up a field of research that connects the quantum mechanical world to the real world.

Overall, recent metrological advances in the investigation of QD structural, morphological, optical, and electronic properties provide new opportunities in bridging various fields including material science, physics, chemistry, biology, and computation science. It has opened exciting new areas of research spanning from fundamental science of QDs to the development of next-generation optoelectronic products of commercial interest including displays, solar cells, catalysis, and sensors.

## Acknowledgements

H.K. and M.E.W. gratefully acknowledge the funding from the Engineering and Physical Sciences Research Council (EPSRC, EP/P027628/1). B.H. acknowledges the financial support by the Cardiff University.

## Conflict of Interest

The authors declare no conflict of interest.

## Keywords

microscopy, quantum dots, spatially resolved metrology, spectroscopy, time-resolved metrology

Received: June 30, 2020

Revised: August 19, 2020

Published online:

[1] Y. Shirasaki, G. J. Supran, M. G. Bawendi, V. Bulović, *Nat. Photonics* **2013**, 7, 13.

- [2] J. M. Pietryga, Y.-S. Park, J. Lim, A. F. Fidler, W. K. Bae, S. Brovelli, V. I. Klimov, *Chem. Rev.* **2016**, *116*, 10513.
- [3] L. Brus, *J. Phys. Chem.* **1986**, *90*, 2555.
- [4] S. B. Brichkin, V. F. Razumov, *Russ. Chem. Rev.* **2016**, *85*, 1297.
- [5] A. P. Alivisatos, *Science* **1996**, *271*, 933.
- [6] A. M. Smith, S. Nie, *Acc. Chem. Res.* **2010**, *43*, 190.
- [7] U. Resch-Genger, M. Grabolle, S. Cavaliere-Jaricot, R. Nitschke, T. Nann, *Nat. Methods* **2008**, *5*, 763.
- [8] G. Konstantatos, in *Colloidal Quantum Dot Optoelectronics and Photovoltaics* (Eds: G. Konstantatos, E. H. Sargent), Cambridge University Press, Cambridge **2013**, pp. 173–198.
- [9] D. Bera, L. Qian, T. Tseng, P. H. Holloway, *Materials* **2010**, *3*, 2260.
- [10] B. Li, M. Lu, J. Feng, J. Zhang, P. M. Smowton, J. I. Sohn, I.-K. Park, H. Zhong, B. Hou, *J. Mater. Chem. C* **2020**, *8*, 10676.
- [11] W. W. Yu, X. Peng, *Angew. Chem., Int. Ed.* **2002**, *41*, 2368.
- [12] O. I. Mičić, A. J. Nozik, *J. Lumin.* **1996**, *70*, 95.
- [13] G. I. Maikov, R. Vaxenburg, A. Sashchiuk, E. Lifshitz, *ACS Nano* **2010**, *4*, 6547.
- [14] S. Cao, J. Zheng, J. Zhao, Z. Yang, M. Shang, C. Li, W. Yang, X. Fang, *Adv. Funct. Mater.* **2016**, *26*, 7224.
- [15] X. Fang, T. Zhai, U. K. Gautam, L. Li, L. Wu, Y. Bando, D. Golberg, *Prog. Mater. Sci.* **2011**, *56*, 175.
- [16] X. Xu, L. Hu, N. Gao, S. Liu, S. Wageh, A. A. Al-Ghamdi, A. Alshahrie, X. Fang, *Adv. Funct. Mater.* **2015**, *25*, 445.
- [17] K. Boldt, N. Kirkwood, G. A. Beane, P. Mulvaney, *Chem. Mater.* **2013**, *25*, 4731.
- [18] M. A. Hines, P. Guyot-Sionnest, *J. Phys. Chem.* **1996**, *100*, 468.
- [19] B. O. Dabbousi, J. Rodriguez-Viejo, F. V. Mikulec, J. R. Heine, H. Mattoussi, R. Ober, K. F. Jensen, M. G. Bawendi, *J. Phys. Chem. B* **1997**, *101*, 9463.
- [20] S. Kim, B. Fisher, H.-J. Eisler, M. Bawendi, *J. Am. Chem. Soc.* **2003**, *125*, 11466.
- [21] R. Osovsky, D. Cheskis, V. Kloper, A. Sashchiuk, M. Kroner, E. Lifshitz, *Phys. Rev. Lett.* **2009**, *102*, 197401.
- [22] R. Xie, X. Peng, *Angew. Chem., Int. Ed.* **2008**, *47*, 7677.
- [23] L. Langof, L. Fradkin, E. Ehrenfreund, E. Lifshitz, O. I. Micic, A. J. Nozik, *Chem. Phys.* **2004**, *297*, 93.
- [24] S. Xu, J. Ziegler, T. Nann, *J. Mater. Chem.* **2008**, *18*, 2653.
- [25] E. Lifshitz, M. Brumer, A. Kigel, A. Sashchiuk, M. Bashouti, M. Sirota, E. Galun, Z. Burshtein, A. Q. Le Quang, I. Ledoux-Rak, *J. Zyss, J. Phys. Chem. B* **2006**, *110*, 25356.
- [26] R. Toufanian, A. Piryatinski, A. H. Mahler, R. Iyer, J. A. Hollingsworth, A. M. Dennis, *Front. Chem.* **2018**, *6*, 567.
- [27] N. Mishra, V. G. Vasavi Dutt, M. P. Arciniegas, *Chem. Mater.* **2019**, *31*, 9216.
- [28] N. Mishra, W. Y. Wu, B. M. Srinivasan, R. Hariharaputran, Y. W. Zhang, Y. Chan, *Chem. Mater.* **2016**, *28*, 1187.
- [29] N. Mishra, B. Mukherjee, G. Xing, S. Chakraborty, A. Guchhait, J. Y. Lim, *Nanoscale* **2016**, *8*, 14203.
- [30] R. Koole, E. Groeneveld, D. Vanmaekelbergh, A. Meijerink, in *Nanoparticles* (Ed. C. de Mello Donegá), Springer, Berlin **2014**, pp. 13–51.
- [31] V. I. Klimov, *Annu. Rev. Phys. Chem.* **2007**, *58*, 635.
- [32] D. A. Wheeler, J. Z. Zhang, *Adv. Mater.* **2013**, *25*, 2878.
- [33] S. W. Tong, N. Mishra, C. L. Su, Y. Nalla, W. Wu, W. Ji, J. Zhang, Y. Chan, K. P. Loh, *Adv. Funct. Mater.* **2014**, *24*, 1904.
- [34] M. D. Peterson, L. C. Cass, R. D. Harris, K. Edme, K. Sung, E. A. Weiss, *Annu. Rev. Phys. Chem.* **2014**, *65*, 317.
- [35] K. Wei, X. Zheng, X. Cheng, C. Shen, T. Jiang, *Adv. Opt. Mater.* **2016**, *4*, 1993.
- [36] B. Hou, B. Kim, H. K. H. Lee, Y. Cho, P. Giraud, M. Liu, J. Zhang, M. L. Davies, J. R. Durrant, W. C. Tsoi, Z. Li, S. D. Dimitrov, J. I. Sohn, S. Cha, J. M. Kim, *Adv. Funct. Mater.* **2020**, 2004563.
- [37] G. E. Cragg, A. L. Efros, *Nano Lett.* **2010**, *10*, 313.
- [38] M. Nirmal, B. O. Dabbousi, M. G. Bawendi, J. J. Macklin, J. K. Trautman, T. D. Harris, L. E. Brus, *Nature* **1996**, *383*, 802.
- [39] A. L. Efros, D. J. Nesbitt, *Nat. Nanotechnol.* **2016**, *11*, 661.
- [40] H. Zhu, T. Lian, *Energy Environ. Sci.* **2012**, *5*, 9406.
- [41] K. Wu, W. E. Rodríguez-Córdoba, Z. Liu, H. Zhu, T. Lian, *ACS Nano* **2013**, *7*, 7173.
- [42] N. Mishra, N. J. Orfield, F. Wang, Z. Hu, S. Krishnamurthy, A. V. Malko, J. L. Casson, H. Htoon, M. Sykora, J. A. Hollingsworth, *Nat. Commun.* **2017**, *8*, 15083.
- [43] Y. Jang, A. Shapiro, M. Isarov, A. Rubin-Brusilovski, A. Safran, A. K. Budniak, F. Horani, J. Dehnell, A. Sashchiuk, E. Lifshitz, *Chem. Commun.* **2017**, 1002.
- [44] M. R. Kim, D. Ma, *J. Phys. Chem. Lett.* **2015**, *6*, 85.
- [45] G. S. Selopal, H. Zhao, Z. M. Wang, F. Rosei, *Adv. Funct. Mater.* **2020**, *30*, 2070086.
- [46] G. Konstantatos, I. Howard, A. Fischer, S. Hoogland, J. Clifford, E. Klem, L. Levina, E. H. Sargent, *Nature* **2006**, *442*, 180.
- [47] J. Drbohlavova, V. Adam, R. Kizek, J. Hubalek, *Int. J. Mol. Sci.* **2009**, *10*, 656.
- [48] X. Dai, Y. Deng, X. Peng, Y. Jin, *Adv. Mater.* **2017**, *29*, 1607022.
- [49] T. H. Kim, K. S. Cho, E. K. Lee, S. J. Lee, J. Chae, J. W. Kim, D. H. Kim, J. Y. Kwon, G. Amaratunga, S. Y. Lee, B. L. Choi, Y. Kuk, J. M. Kim, K. Kim, *Nat. Photonics* **2011**, *5*, 176.
- [50] B. Hou, Y. Cho, B. S. Kim, J. Hong, J. B. Park, S. J. Ahn, J. I. Sohn, S. Cha, J. M. Kim, *ACS Energy Lett.* **2016**, *1*, 834.
- [51] M. J. Choi, F. P. García de Arquer, A. H. Proppe, A. Seifitokaldani, J. Choi, J. Kim, S. W. Baek, M. Liu, B. Sun, M. Biondi, B. Scheffel, G. Walters, D. H. Nam, J. W. Jo, O. Ouellette, O. Voznyy, S. Hoogland, S. O. Kelley, Y. S. Jung, E. H. Sargent, *Nat. Commun.* **2020**, *11*, 1.
- [52] F. Prins, M. Buscema, J. S. Seldenthuis, S. Etaki, G. Buchs, M. Barkelid, V. Zwiller, Y. Gao, A. J. Houtepen, L. D. A. Siebbeles, H. S. J. van der Zant, *Nano Lett.* **2012**, *12*, 5740.
- [53] J. P. Clifford, G. Konstantatos, K. W. Johnston, S. Hoogland, L. Levina, E. H. Sargent, *Nat. Nanotechnol.* **2009**, *4*, 40.
- [54] P. Zhao, Q. Xu, J. Tao, Z. Jin, Y. Pan, C. Yu, Z. Yu, *Wiley Interdiscip. Rev.: Nanomed. Nanobiotechnol.* **2018**, *10*, e1483.
- [55] C. Li, W. Li, H. Liu, Y. Zhang, G. Chen, Z. Li, Q. Wang, *Angew. Chem., Int. Ed.* **2020**, *59*, 247.
- [56] G. Lv, W. Guo, W. Zhang, T. Zhang, S. Li, S. Chen, A. S. Eltahan, D. Wang, Y. Wang, J. Zhang, P. C. Wang, J. Chang, X.-J. Liang, *ACS Nano* **2016**, *10*, 9637.
- [57] M. R. Buck, R. E. Schaak, *Angew. Chem., Int. Ed.* **2013**, *52*, 6154.
- [58] S. G. Kwon, T. Hyeon, *Small* **2011**, *7*, 2685.
- [59] J. M. Yuk, J. Park, P. Ercius, K. Kim, D. J. Hellebusch, M. F. Crommie, J. Y. Lee, A. Zettl, A. P. Alivisatos, *Science* **2012**, *336*, 61.
- [60] H. Wen, M. J. Cherukara, M. V. Holt, *Annu. Rev. Mater. Res.* **2019**, *49*, 389.
- [61] H. J. W. Zandvliet, A. van Houselt, *Annu. Rev. Anal. Chem.* **2009**, *2*, 37.
- [62] G. H. Campbell, J. T. McKeown, M. K. Santala, *Appl. Phys. Rev.* **2014**, *1*, 041101.
- [63] T. L. Cocker, D. Peller, P. Yu, J. Repp, R. Huber, *Nature* **2016**, *539*, 263.
- [64] J. I. Goldstein, D. E. Newbury, J. R. Michael, N. W. M. Ritchie, J. H. J. Scott, D. C. Joy, *Scanning Electron Microscopy and X-Ray Microanalysis*, Springer, New York **2018**.
- [65] G. Guzzinati, T. Altantzis, M. Batuk, A. De Backer, G. Lumbeeck, V. Samaee, D. Batuk, H. Idrissi, J. Hadermann, S. Van Aert, D. Schryvers, J. Verbeeck, S. Bals, *Materials* **2018**, *11*, 1304.
- [66] S. U. Nanayakkara, J. van de Lagemaat, J. M. Luther, *Chem. Rev.* **2015**, *115*, 8157.
- [67] C. Coman, L. F. Leopold, in *Raman Spectroscopy and Applications* (Ed: M. Khan), InTech, London **2017**.
- [68] B. Abécassis, C. Bouet, C. Garnerio, D. Constantin, N. Lequeux, S. Ithurria, B. Dubertret, B. R. Pauw, D. Pontoni, *Nano Lett.* **2015**, *15*, 2620.
- [69] P. Kambhampati, *Acc. Chem. Res.* **2011**, *44*, 1.

- [70] E. P. Farr, J. C. Quintana, V. Reynoso, J. D. Ruberry, W. R. Shin, K. R. Swartz, *J. Chem. Educ.* **2018**, *95*, 864.
- [71] R. Berera, R. van Grondelle, J. T. M. Kennis, *Photosynth. Res.* **2009**, *101*, 105.
- [72] C. T. Smith, M. A. Leontiadou, R. Page, P. O'Brien, D. J. Binks, *Adv. Sci.* **2015**, *2*, 1500088.
- [73] M. Jones, G. D. Scholes, *J. Mater. Chem.* **2010**, *20*, 3533.
- [74] E. M. Y. Lee, W. A. Tisdale, *J. Phys. Chem. C* **2015**, *119*, 9005.
- [75] Y. Liao, G. Xing, N. Mishra, T. C. Sum, Y. Chan, *Adv. Mater.* **2012**, *24*, OP159.
- [76] H. Zhu, N. Song, T. Lian, *J. Am. Chem. Soc.* **2011**, *133*, 8762.
- [77] P. Peng, D. J. Milliron, S. M. Hughes, J. C. Johnson, A. P. Alivisatos, R. J. Saykally, *Nano Lett.* **2005**, *5*, 1809.
- [78] M. G. Lupo, F. Della Sala, L. Carbone, M. Zavelani-Rossi, A. Fiore, L. Lüer, D. Polli, R. Cingolani, L. Manna, G. Lanzani, *Nano Lett.* **2008**, *8*, 4582.
- [79] Z. Deusch, L. Neeman, D. Oron, *Nat. Nanotechnol.* **2013**, *8*, 649.
- [80] H. Xu, V. Chmyrov, J. Widengren, H. Brismar, Y. Fu, *Phys. Chem. Chem. Phys.* **2015**, *17*, 27588.
- [81] A. H. Flayyih, A. H. Al-Khursan, *J. Phys. D: Appl. Phys.* **2013**, *46*, 445102.
- [82] A. I. McIntosh, B. Yang, S. M. Goldup, M. Watkinson, R. S. Donnan, *Chem. Soc. Rev.* **2012**, *41*, 2072.
- [83] J. R. McBride, N. Mishra, S. M. Click, N. J. Orfield, F. Wang, K. Acharya, M. F. Chisholm, H. Htoon, S. J. Rosenthal, J. A. Hollingsworth, *J. Chem. Phys.* **2020**, *152*, 124713.
- [84] M. S. Mehata, R. K. Ratnesh, *Dalton Trans.* **2019**, *48*, 7619.
- [85] A. Javier, D. Magana, T. Jennings, G. F. Strouse, *Appl. Phys. Lett.* **2003**, *83*, 1423.
- [86] U. Kaiser, D. Jimenez de Aberasturi, R. Malinowski, F. Amin, W. J. Parak, W. Heimbrot, *Appl. Phys. Lett.* **2014**, *104*, 041901.
- [87] B. Omogo, F. Gao, P. Bajwa, M. Kaneko, C. D. Heyes, *ACS Nano* **2016**, *10*, 4072.
- [88] C. R. Kagan, C. B. Murray, M. G. Bawendi, *Phys. Rev. B* **1996**, *54*, 8633.
- [89] Q. Lin, L. Wang, Z. Li, H. Shen, L. Guo, Y. Kuang, H. Wang, L. S. Li, *ACS Photonics* **2018**, *5*, 939.
- [90] B. N. Pal, Y. Ghosh, S. Brovelli, R. Laocharoensuk, V. I. Klimov, J. A. Hollingsworth, H. Htoon, *Nano Lett.* **2012**, *12*, 331.
- [91] X. Dai, Z. Zhang, Y. Jin, Y. Niu, H. Cao, X. Liang, L. Chen, J. Wang, X. Peng, *Nature* **2014**, *515*, 96.
- [92] Z. Zhang, Y. Ye, C. Pu, Y. Deng, X. Dai, X. Chen, D. Chen, X. Zheng, Y. Gao, W. Fang, X. Peng, Y. Jin, *Adv. Mater.* **2018**, *30*, 1801387.
- [93] A. M. Dennis, B. D. Mangum, A. Piryatinski, Y. S. Park, D. C. Hannah, J. L. Casson, D. J. Williams, R. D. Schaller, H. Htoon, J. A. Hollingsworth, *Nano Lett.* **2012**, *12*, 5545.
- [94] R. D. Schaller, M. Sykora, S. Jeong, V. I. Klimov, *J. Phys. Chem. B* **2006**, *110*, 25332.
- [95] S. A. Ivanov, M. Achermann, *ACS Nano* **2010**, *4*, 5994.
- [96] M. Jones, S. S. Lo, G. D. Scholes, *J. Phys. Chem. C* **2009**, *113*, 18632.
- [97] A. Y. Kuposov, P. Szymanski, T. Cardolaccia, T. J. Meyer, V. I. Klimov, M. Sykora, *Adv. Funct. Mater.* **2011**, *21*, 3159.
- [98] A. W. Achtstein, O. Marquardt, R. Scott, M. Ibrahim, T. Riedl, A. V. Prudnikau, A. Antanovich, N. Owschimikow, J. K. N. Lindner, M. Artemyev, U. Woggon, *ACS Nano* **2018**, *12*, 9476.
- [99] S. Rawalekar, S. Kaniyankandy, S. Verma, H. N. Ghosh, *J. Phys. Chem. C* **2010**, *114*, 1460.
- [100] H. Wang, C. De Mello Donegá, A. Meijerink, M. Glasbeek, *J. Phys. Chem. B* **2006**, *110*, 733.
- [101] B. Zhang, X. Wang, D. Wang, J. Tang, X. Fang, D. Fang, X. Wang, R. Chen, T. He, Z. Wei, *J. Phys. Chem. C* **2019**, *123*, 27207.
- [102] C. Burda, S. Link, M. Mohamed, M. El-Sayed, *J. Phys. Chem. B* **2001**, *105*, 12286.
- [103] S. L. Sewall, R. R. Cooney, K. E. H. Anderson, E. A. Dias, D. M. Sagar, P. Kambhampati, *J. Chem. Phys.* **2008**, *129*, 084701.
- [104] V. I. Klimov, D. W. McBranch, C. A. Leatherdale, M. G. Bawendi, *Phys. Rev. B* **1999**, *60*, 13740.
- [105] V. I. Klimov, A. A. Mikhailovsky, D. W. McBranch, C. A. Leatherdale, M. G. Bawendi, *Phys. Rev. B* **2000**, *61*, R13349.
- [106] V. Chikan, D. F. Kelley, *Nano Lett.* **2002**, *2*, 141.
- [107] Y. Yan, L. Wang, C. B. Vaughn, G. Chen, P. G. Van Patten, *J. Phys. Chem. C* **2011**, *115*, 24521.
- [108] M. O'Neil, J. Marohn, G. McLendon, *Chem. Phys. Lett.* **1990**, *168*, 208.
- [109] S. Logunov, T. Green, S. Marguet, M. A. El-Sayed, *J. Phys. Chem. A* **1998**, *102*, 5652.
- [110] Y. Yan, G. Chen, P. G. Van Patten, *J. Phys. Chem. C* **2011**, *115*, 22717.
- [111] J. I. Wong, N. Mishra, G. Xing, M. Li, S. Chakraborty, T. C. Sum, Y. Shi, Y. Chan, H. Y. Yang, *ACS Nano* **2014**, *8*, 2873.
- [112] P. Kambhampati, *J. Phys. Chem. C* **2011**, *115*, 22089.
- [113] S. Taguchi, M. Saruyama, T. Teranishi, Y. Kanemitsu, *Phys. Rev. B* **2011**, *83*, 155324.
- [114] K. Wu, G. Liang, D. Kong, J. Chen, Z. Chen, X. Shan, J. R. McBride, T. Lian, *Chem. Sci.* **2016**, *7*, 1238.
- [115] L. Wang, K. Nonaka, T. Okuhata, T. Katayama, N. Tamai, *J. Phys. Chem. C* **2018**, *122*, 12038.
- [116] B. Hou, *Isr. J. Chem.* **2019**, *59*, 637.
- [117] Y. Chen, J. Vela, H. Htoon, J. L. Casson, J. Donald, D. A. Bussian, V. I. Klimov, J. A. Hollingsworth, D. J. Werder, *J. Am. Chem. Soc.* **2008**, *130*, 5026.
- [118] M. Hamada, S. Nakanishi, T. Itoh, M. Ishikawa, V. Biju, *ACS Nano* **2010**, *4*, 4445.
- [119] W. Koh, D. Kim, J. Kim, *Nanoscale* **2016**, *8*, 16405.
- [120] C. Galland, Y. Ghosh, A. Steinbrück, M. Sykora, J. A. Hollingsworth, V. I. Klimov, H. Htoon, *Nature* **2011**, *479*, 203.
- [121] B. Diaconescu, L. A. Padilha, P. Nagpal, B. S. Swartzentruber, V. I. Klimov, *Phys. Rev. Lett.* **2013**, *110*, 127406.
- [122] P. Liljeroth, P. A. Z. van Emmichoven, S. G. Hickey, H. Weller, B. Grandier, G. Allan, D. Vanmaekelbergh, *Phys. Rev. Lett.* **2005**, *95*, 086801.
- [123] T. Wang, R. Vaxenburg, W. Liu, S. M. Rupich, E. Lifshitz, A. L. Efros, D. V. Talapin, S. J. Sibener, *ACS Nano* **2015**, *9*, 725.
- [124] I. Swart, Z. Sun, D. Vanmaekelbergh, P. Liljeroth, *Nano Lett.* **2010**, *10*, 1931.
- [125] O. Millo, D. Katz, Y. Cao, U. Banin, *Phys. Rev. Lett.* **2001**, *86*, 5751.
- [126] D. A. Kisilitsyn, C. F. Gervasi, T. Allen, P. K. B. Palomaki, J. D. Hackley, R. Maruyama, G. V. Nazin, *J. Phys. Chem. Lett.* **2014**, *5*, 3701.
- [127] C. F. Gervasi, D. A. Kisilitsyn, T. L. Allen, J. D. Hackley, R. Maruyama, G. V. Nazin, *Nanoscale* **2015**, *7*, 19732.
- [128] T. Walther, *J. Microsc.* **2015**, *257*, 171.
- [129] B. Fultz, J. Howe, *Transmission Electron Microscopy and Diffractometry of Materials*, Springer, Berlin **2013**.
- [130] C.-P. Liu, P. D. Miller, W. L. Henstrom, J. M. Gibson, *J. Microsc.* **2000**, *199*, 130.
- [131] B. Hou, M. Sohn, Y.-W. Lee, J. Zhang, J. I. Sohn, H. Kim, S. Cha, J. M. Kim, *Nano Energy* **2019**, *62*, 764.
- [132] B. Hou, S.-H. Jung, J. Zhang, Y. Hong, B.-S. Kim, J. I. Sohn, E. K. Lee, B. L. Choi, D. Whang, S. Cha, J. M. Kim, *Appl. Phys. Lett.* **2019**, *114*, 243104.
- [133] N. Kattan, B. Hou, D. J. Fermín, D. Cherns, *Appl. Mater. Today* **2015**, *1*, 52.
- [134] B. Hou, D. Parker, G. P. Kissling, J. A. Jones, D. Cherns, D. J. Fermín, *J. Phys. Chem. C* **2013**, *117*, 6814.
- [135] B. Hou, D. Benito-Alifonso, R. Webster, D. Cherns, M. C. Galan, D. J. Fermín, *J. Mater. Chem. A* **2014**, *2*, 6879.
- [136] K. Han, W. Bin Im, J. Heo, W. J. Chung, *Chem. Commun.* **2016**, *52*, 3564.
- [137] H. Müllejjans, J. Bruley, *J. Phys. IV* **1993**, *3*, C7.
- [138] J. Maes, N. Castro, K. De Nolf, W. Walravens, B. Abécassis, Z. Hens, *Chem. Mater.* **2018**, *30*, 3952.

- [139] M. C. Weidman, Q. Nguyen, D. M. Smilgies, W. A. Tisdale, *Chem. Mater.* **2018**, *30*, 807.
- [140] S. A. Wilson, E. Green, I. I. Mathews, M. Benfatto, K. O. Hodgson, B. Hedman, R. Sarangi, *Proc. Natl. Acad. Sci. USA* **2013**, *110*, 16333.
- [141] L. Tian, W. Li, T. Zhu, G. Zhao, X. Liu, *J. Mater. Chem. A* **2019**, *7*, 18480.
- [142] L. J. Tian, Y. Peng, D. L. Chen, J. Y. Ma, H. Q. Yu, W. W. Li, *Sci. Rep.* **2017**, *7*, 1.
- [143] L. J. Tian, Y. Min, W. W. Li, J. J. Chen, N. Q. Zhou, T. T. Zhu, D. B. Li, J. Y. Ma, P. F. An, L. R. Zheng, H. Huang, Y. Z. Liu, H. Q. Yu, *ACS Nano* **2019**, *13*, 5841.
- [144] G. Chen, F. Tian, Y. Zhang, Y. Zhang, C. Li, Q. Wang, *Adv. Funct. Mater.* **2014**, *24*, 2481.
- [145] V. Poderys, M. Matulionyte, A. Selskis, R. Rotomskis, *Nanoscale Res. Lett.* **2010**, *6*, 1.
- [146] P. Kulis, J. Butikova, B. Polyakov, G. Marcins, J. Pervenecka, K. Pudzs, I. Tale, *IOP Conf. Ser.: Mater. Sci. Eng.* **2012**, *38*, 012048.
- [147] T. Yamauchi, M. Tabuchi, A. Nakamura, *Appl. Phys. Lett.* **2004**, *84*, 3834.
- [148] C. H. Ben-Porat, O. Cherniavskaya, L. Brus, K.-S. Cho, C. B. Murray, *J. Phys. Chem. A* **2004**, *108*, 7814.
- [149] S. Shusterman, A. Raizman, A. Sher, Y. Parltiel, A. Schwarzman, E. Lepkifker, Y. Rosenwaks, *Nano Lett.* **2007**, *7*, 2089.
- [150] V. M. Dzhagan, M. Y. Valakh, A. G. Milekhin, N. A. Yeryukov, D. R. T. Zahn, E. Cassette, T. Pons, B. Dubertret, *J. Phys. Chem. C* **2013**, *117*, 18225.
- [151] N. Tschirner, H. Lange, A. Schliwa, A. Biermann, C. Thomsen, K. Lambert, R. Gomes, Z. Hens, *Chem. Mater.* **2012**, *24*, 311.
- [152] V. M. Dzhagan, M. Y. Valakh, A. E. Raevskaya, A. L. Stroyuk, S. Y. Kuchmiy, D. R. T. Zahn, *Appl. Surf. Sci.* **2008**, *255*, 725.
- [153] V. M. Dzhagan, M. Y. Valakh, O. E. Raevska, O. L. Stroyuk, S. Y. Kuchmiy, D. R. T. Zahn, *Nanotechnology* **2009**, *20*, 365704.
- [154] S. Y. Kuchmiy, A. E. Raevskaya, D. R. T. Zahn, M. Y. Valakh, V. M. Dzhagan, A. L. Stroyuk, *Nanotechnology* **2007**, *18*, 285701.
- [155] F. Todescato, A. Minotto, R. Signorini, J. J. Jasieniak, R. Bozio, *ACS Nano* **2013**, *7*, 6649.
- [156] A. V. Baranov, Y. P. Rakovich, J. F. Donegan, T. S. Perova, R. A. Moore, D. V. Talapin, A. L. Rogach, Y. Masumoto, I. Nabiev, *Phys. Rev. B* **2003**, *68*, 165306.
- [157] Y. Pu, F. Cai, D. Wang, J.-X. Wang, J.-F. Chen, *Ind. Eng. Chem. Res.* **2018**, *57*, 1790.
- [158] I. Lokteva, M. Koof, M. Walther, G. Grübel, F. Lehmkuhler, *Small* **2019**, *15*, 1900438.
- [159] S. T. Skowron, T. W. Chamberlain, J. Biskupek, U. Kaiser, E. Besley, A. N. Khlobystov, *Acc. Chem. Res.* **2017**, *50*, 1797.
- [160] B. Goris, M. A. Van Huis, S. Bals, H. W. Zandbergen, L. Manna, G. Van Tendeloo, *Small* **2012**, *8*, 937.
- [161] A. O. Yalcin, B. Goris, R. J. A. van Dijk-Moes, Z. Fan, A. K. Erdamar, F. D. Tichelaar, T. J. H. Vlugt, G. Van Tendeloo, S. Bals, D. Vanmaekelbergh, H. W. Zandbergen, M. A. van Huis, *Chem. Commun.* **2015**, *51*, 3320.
- [162] J. P. Patterson, Y. Xu, M.-A. Moradi, N. A. J. M. Sommerdijk, H. Friedrich, *Acc. Chem. Res.* **2017**, *50*, 1495.
- [163] Z. Zeng, W. Zheng, H. Zheng, *Acc. Chem. Res.* **2017**, *50*, 1808.
- [164] J. Huang, Z. Huang, Y. Yang, H. Zhu, T. Lian, *J. Am. Chem. Soc.* **2010**, *132*, 4858.
- [165] C.-H. Chuang, T. L. Doane, S. S. Lo, G. D. Scholes, C. Burda, *ACS Nano* **2011**, *5*, 6016.
- [166] H. H. Fielding, G. A. Worth, *Chem. Soc. Rev.* **2018**, *47*, 309.
- [167] W. Xiong, D. D. Hickstein, K. J. Schnitzenbaumer, J. L. Ellis, B. B. Palm, K. E. Keister, C. Ding, L. Miaja-Avila, G. Dukovic, J. L. Jimenez, M. M. Murnane, H. C. Kapteyn, *Nano Lett.* **2013**, *13*, 2924.
- [168] O. Mandula, M. Elzo Aizarna, J. Eymery, M. Burghammer, V. Favre-Nicolin, *J. Appl. Crystallogr.* **2016**, *49*, 1842.
- [169] C. Wang, U. Steiner, A. Sepe, *Small* **2018**, *14*, 1802291.
- [170] D. Nguyen, J. J. Goings, H. A. Nguyen, J. Lyding, X. Li, M. Gruebele, *J. Chem. Phys.* **2018**, *148*, 064701.
- [171] Y. Terada, S. Yoshida, O. Takeuchi, H. Shigekawa, *Nat. Photonics* **2010**, *4*, 869.
- [172] E. Nakamura, *Acc. Chem. Res.* **2017**, *50*, 1281.



**Hasna Kudilatt** is a research associate in the Department of Engineering at the University of Cambridge. She received her Ph.D. degree from Cochin University of Science and Technology, India. She worked as an assistant professor of Physics at the Department of Collegiate Education, Government of Kerala, India. Her research interests include quantum dots, optoelectronic devices, plasmonics, and surface-enhanced Raman spectroscopy.



**Bo Hou** is a lecturer in the School of Physics and Astronomy at the Cardiff University. He received his Ph.D. degree from the University of Bristol (2010–2014). He worked as a postdoctoral researcher at the University of Oxford (2014–2018, Wolfson College) and as a senior research fellow at the University of Cambridge (2018–2020, St. Edmund's College). His research interests include QD synthesis, QD optoelectronics, electron microscopy (TEM), and dynamic charge transfer analysis.



**Mark E. Welland** is a professor of Nanotechnology at the University of Cambridge. He is the head of the Cambridge Nanoscience Centre, director of the Maxwell Centre, deputy vice-chancellor and special adviser on China, and master of St Catharine's College. He received his Ph.D. degree from the University of Bristol, and he is a world leader in nanotechnology and scanned probe microscopy. His current research interest includes protein misfolding problems related to human diseases such as Alzheimer's, nanostructured materials for high efficiency low-cost solar cells, biologically-inspired nanomaterials for green technologies, and nanoelectronics for future generation communications and sensing.